Revisiting Axion-Like Particle Couplings to Electroweak Gauge Bosons*

Jin Sun (孙进)[2†] Zhi-Peng Xing (邢志鹏)[1‡] Seokhoon Yun[2§]

[1]Department of Physics and Institute of Theoretical Physics, Nanjing Normal University, Nanjing, Jiangsu 210023, China
[2]Particle Theory and Cosmology Group, Center for Theoretical Physics of the Universe, Institute for Basic Science (IBS), Daejeon 34126, Korea

Abstract: Motivated by the more and more abundant experimental data, we revisit the couplings of axion-like particle (ALP) to electroweak gauge bosons across the ALP mass range from MeV to 100 GeV. We extend both current and projected experimental limits on these couplings, including the ALP couplings with W-boson g_{aW} and hypercharge B-boson g_{aB}. To clarify the contributions from electroweak boson couplings, we analyze and compare the resulting effects for various values of g_{aW} and g_{aB}. The couplings induce flavor-conserving ALP interactions with Standard Model (SM) fermions at the one-loop level, while g_{aW} additionally gives rise to flavor-changing ALP-quark couplings. These phenomena warrant further investigation through rare meson decays and neutral meson mixing processes, particularly in light of recent results from $B^+ \to K^+\nu\bar{\nu}$ and $K^+ \to \pi^+\nu\bar{\nu}$. We find that the rare two-body decays of pseudoscalar mesons offer the most sensitive probes below the kinematic threshold. In the high-mass region, complementary bounds arise from Pb-Pb collision and Z-boson measurements, including the invisible decay $Z \to a\gamma$ with subsequent ALP decays and constraints from oblique parameters (S, T, U). Future lepton colliders, such as CEPC and FCC-ee operating at the Z-pole, along with SHiP, provide further opportunities to probe ALP couplings to electroweak gauge bosons.

Keywords: Axion like particle, FCNC, B Meson

DOI: **CSTR:** 32044.14.ChinesePhysicsC.

I. INTRODUCTION

Probing new pseudoscalar particles with masses below the electroweak scale, predicted in some well-motivated extensions of the Standard Model (SM), plays an important role in particle physics. A notable example is Axion-like particles (ALPs), an extension of original quantum chromodynamics (QCD) axion from spontaneous breaking of Peccei-Quinn symmetry [1−6]. As a generalization, ALP can be realized in a variety of new physics scenarios with a significantly larger parameter space, see e.g. [7−10] for a review. This enables a rich phenomenology, investigated in both low-energy [11−14] and high-energy experiments [15−17]. Additionally, many new experiments are conducted, including IBS-CAPP MAX [18], Oscillating Resonant Group AxioN (ORGAN) [19], Any Light Particle Search II (ALPS II) [20], CERN Axion Solar Telescope (CAST) [21], and NEON [22].

In recent years, increasingly precise predictions [23−36] and experimental observations [37] for meson flavor-changing neutral current (FCNC) decays have revealed several notable discrepancies. For example, Belle-II uses an integrated luminosity 362 fb^{-1} to measure $\mathrm{Br}(B^+ \to K^+\nu\bar{\nu}) = 23 \pm 5^{+5}_{-4}$, exceeding the SM prediction by 2.7σ significance [38]. Similarly, the NA62 collaboration [39, 40] has reported precise measurements of the branching ratio $\mathrm{Br}(K^+ \to \pi^+\nu\bar{\nu})$, significantly improving upon the previous results from the E949 experiment [41]. Due to the presence of invisible final-state neutrinos, these decay signals could be mimicked by ALP, which would appear as missing-energy events. Table 2 summarizes recent results and refined experimental upper limits for meson decays from various experiments, which motivate us to update and extend previous analyses on meson FCNC processes involving an ALP. Several mechanisms have been proposed to construct flavor-changing ALP interactions [42−50]. In particular, ALP interactions with $W^\pm$ bosons can induce FCNC processes at one loop level [44], which constitutes the primary focus of this

Received 21 May 2025; Accepted 23 July 2025

* This work was supported by IBS under the project code, IBS-R018-D1. This work is supported by NSFC under grants No. 12375088, 12335003 and 12405113

† E-mail: sunjin0810@ibs.re.kr
‡ E-mail: Zhi-Peng Xing, zpxing@nnu.edu.cn(corresponding author)
§ E-mail: seokhoon.yun@ibs.re.kr

work.

In this paper, we provide an updated and extended analysis on the experimental limits of the ALP couplings to electroweak gauge bosons across the ALP mass range from MeV to 100 GeV. As mentioned, the ALP-$W^{\pm}$ couplings give rise to flavor-changing ALP-quark interactions $q_i - q_j - a$ at the one-loop level. The associated physical processes, such as rare meson decays and neutral meson mixing, are analyzed to determine excluded regions in the ALP parameter space with the state-of-the-art SM predictions and new experimental data. Pb-Pb collisions also provide constraints in the ALP mass range $m_a \in [5, 100]$ GeV. Additionally, these couplings affect Z-boson precision measurements, including Γ_Z, $Z \to \gamma a$ with subsequent decays, and the oblique parameters (S, T, U). Moreover, we analyze future experimental sensitivities from lepton colliders (e.g., CEPC and FCC-ee) operating at the Z-pole and the proposed SHiP experiment. To provide a comprehensive basis for comparison, we consider four distinctive scenarios from two independent ALP couplings, namely the ALP-$SU(2)_L$ gauge boson coupling g_{aW} and the ALP-hypercharge gauge boson coupling g_{aB},

- $g_{a\gamma\gamma} = 0$: suppress ALP-photon interaction by cancellation between g_{aW} and g_{aB}, called photophobic ALP [51];
- $g_{aB} = 0$: turn off the coupling with $U(1)_Y$ field;
- $g_{aB} * g_{aW} > 0$: the same sign to enhance the ALP-photon coupling;
- $g_{aW} = 0$: turn off the coupling with $SU(2)_L$ field.

The rest of the paper is organized as follows. In section II, we discuss low energy effective couplings of an ALP induced from the ALP couplings to electroweak gauge bosons at a UV scale. Section III presents a comprehensive list of phenomenological observables relevant for probing the ALP couplings to electroweak gauge bosons. In section IV, we show our results on current and future experimental limits on the ALP-electroweak gauge boson couplings. We give our conclusions in section V.

II. ALP INTERACTIONS WITH ELECTROWEAK GAUGE BOSONS

The general ALP couplings with gauge bosons are written as

$$\mathcal{L}_{EW} = -\frac{g_{aW}}{4} a W^a_{\mu\nu} \tilde{W}^{a\mu\nu} - \frac{g_{aB}}{4} a B_{\mu\nu} \tilde{B}^{\mu\nu} , \tag{1}$$

where a=1,2,3 represents the SU(2) index, $W^{\mu\nu}$ ($B^{\mu\nu}$) means $SU(2)_L$ ($U(1)_Y$) gauge bosons. $\tilde{W}^{\mu\nu}(\tilde{B}^{\mu\nu})$ are the dual field strength tensors. After symmetry breaking, the fields W and B are transformed into the physical fields γ and Z,

$$B_\mu = c_W A_\mu - s_W Z_\mu , \quad W^3_\mu = s_W A_\mu + c_W Z_\mu , \tag{2}$$

where $c_W \equiv \cos\theta_W$ and $s_W \equiv \sin\theta_W$ with θ_W being the weak Weinberg mixing angle. Adopting the above transformation in Eq. (1), the ALP-gauge boson interactions can be written as

$$\begin{aligned} &-\frac{a}{4}(g_{a\gamma\gamma} F_{\mu\nu}\tilde{F}^{\mu\nu} + g_{a\gamma Z} F_{\mu\nu}\tilde{Z}^{\mu\nu} + g_{aZZ} Z_{\mu\nu}\tilde{Z}^{\mu\nu} \\ &+ g_{aWW} W^+_{\mu\nu}\tilde{W}^{+\mu\nu}) , \end{aligned} \tag{3}$$

where $F_{\mu\nu}$, $W_{\mu\nu}$, and $Z_{\mu\nu}$ are the field strength tensors of the photon, $W^{\pm}$, and Z bosons, respectively. And the coupling coefficients can be expressed in terms of g_{aW} and g_{aB}

$$\begin{aligned} &g_{a\gamma\gamma} = g_{aW} s_W^2 + g_{aB} c_W^2 , \quad g_{a\gamma Z} = 2 c_W s_W (g_{aW} - g_{aB}) , \\ &g_{aZZ} = g_{aW} c_W^2 + g_{aB} s_W^2 . \end{aligned} \tag{4}$$

In addition, the ALP-$W^{\pm}$ couplings arises the following interaction vertex

$$-i g_{aW} p_{W\alpha} p_{W\beta} \epsilon^{\mu\nu\alpha\beta} a W_\mu W_\nu , \tag{5}$$

where $p_{W\alpha}$ and $p_{W\beta}$ mean the four momentum of the W bosons. The a-W-W interaction could contribute to the flavor-changing down-quark interaction as shown in Fig. 1.

Additionally, the SM charged vector-current interaction mediated by $W^{\pm}$ bosons are expressed by

$$\mathcal{L}_W = -\frac{g}{\sqrt{2}} (\bar{u}_L, \bar{c}_L, \bar{t}_L) \gamma^\mu V_{CKM} \begin{pmatrix} d_L \\ s_L \\ b_L \end{pmatrix} W^+_\mu + \text{H.c.}, \tag{6}$$

where g means the gauge coupling constant of $SU(2)_L$ gauge group. And the subscript L means the projection on the left. And the CKM mixing matrix V_{CKM} is parameterized by three rotation angles and one phase

$$\begin{pmatrix} c_{12}c_{13} & s_{12}c_{13} & s_{13}e^{-i\delta} \\ -s_{12}c_{23} - c_{12}s_{23}s_{13}e^{i\delta} & c_{12}c_{23} - s_{12}s_{23}s_{13}e^{i\delta} & s_{23}c_{13} \\ s_{12}s_{23} - c_{12}c_{23}s_{13}e^{i\delta} & -c_{12}s_{23} - s_{12}c_{23}s_{13}e^{i\delta} & c_{23}c_{13} \end{pmatrix} . \tag{7}$$

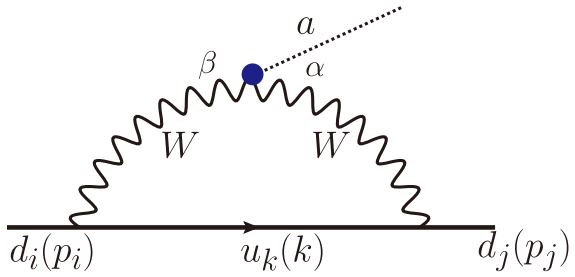

Fig. 1. (color online) The flavor-changing $a-d_i-d_j$ interaction ($i\neq j$). Here the symbols in brackets mean the corresponding momentum.

where the corresponding values are shown in Table 1.

Combing the interactions in Eqs. (5,6), we can write down the amplitude in Fig. 1 as

$$iM = -g_{aW}\frac{g^2}{2}V_{CKM}^{ki}V_{CKM}^{kj*}\int\frac{d^4k}{(2\pi)^4}\bar{u}_j\gamma_\alpha(\not{k}-m_k)\gamma_\beta P_L u_i \times\frac{(k-p_i)_\nu(k-p_j)_\mu\epsilon^{\mu\nu\alpha\beta}}{(k^2-m_k^2)((k-p_j)^2-m_W^2)((k-p_i)^2-m_W^2)}, \quad (8)$$

where $i\neq j$ means the flavor-changing interactions. At first glance, the amplitude should be UV divergences by analyzing the loop integral. After the dimensional regularization, the divergent term should be proportional to

$$div = g_{aW}\frac{g^2}{2}V_{CKM}^{ki}V_{CKM}^{kj*}\frac{i}{4}\frac{\Gamma(2-d/2)}{16\pi^2}\bar{u}_j\gamma_\alpha\gamma^\gamma\gamma_\beta P_L u_i \times[(p_i)_\nu g_{\mu\gamma}+(p_f)_\mu g_{\nu\gamma}]\epsilon^{\mu\nu\alpha\beta}, \quad (9)$$

where $d=4-\epsilon$. This divergence should be eliminated by the Renormalization. Before the renormalization, we can analyze the structure of divergent terms. We found that the divergence term is independent of the quark mass. When summing over the up-type quarks (u,c,t), we naturally obtain the CKM matrix as

$$V_{CKM}^{ui}V_{CKM}^{uj*}+V_{CKM}^{ci}V_{CKM}^{cj*}+V_{CKM}^{ti}V_{CKM}^{tj*}=0. \quad (10)$$

This shows that the divergences disappear due to the unitarity of CKM matrix when we consider the all three generation up-type quark in the propagator.

Ignoring the quark mass of initial and final states and using $\epsilon^{\mu\nu\alpha\beta}\gamma_\nu\gamma_\alpha\gamma_\beta=6i\gamma^\mu\gamma^5$, the finite term with $\bar{u}_j\not{p}_a P_L u_i$ can be obtained approximately as

$$2\int_0^1 dx\int_0^x dy\frac{6}{4(4\pi)^2}\log(1-y+\lambda y) = \frac{3}{4(4\pi)^2}\left(-1+\frac{\lambda(1-\lambda+\lambda\log\lambda)}{(1-\lambda)^2}\right), \quad (11)$$

where $\lambda=m_k^2/m_W^2$. Note that the first term (-1) will also disappear due to the CKM unitarity. Therefore, combining the corresponding coefficients, we obtain the following effective interaction as [42]

$$\mathcal{L}_{d_i\to d_j}\supset -g_{ad_id_j}(\partial_\mu a)\bar{d}_j\gamma^\mu\mathcal{P}_L d_i+\text{H.c.},$$
$$g_{ad_id_j}\equiv-\frac{3\sqrt{2}G_F m_W^2 g_{aW}}{16\pi^2}\sum_{\alpha\in u,c,t}V_{\alpha i}V_{\alpha j}^* f(m_\alpha^2/m_W^2),$$
$$f(x)\equiv\frac{x[1+x(\log x-1)]}{(1-x)^2}, \quad (12)$$

where $G_F=1.1664\times10^{-5}\text{GeV}^{-2}$ is the Fermi constant. V_{ij} means the relevant Cabibbo-Kobayashi-Maskawa (CKM) matrix. Note that for $x\ll1$, we obtain

$$\lim_{x\to0}f(x)=x\,. \quad (13)$$

Note that the interaction is proportional to m_α^2/m_W^2 for $m_\alpha << m_W$.

Therefore, for the above flavor-changing couplings, the results is finite and only depends on the IR value of the effective coupling. Although the individual diagram in Fig. 1 are UV divergent, the divergences will cancel out when summed up intermediate up-type quark flavors u_k. This interesting feature is benefit from the two points: the unitarity of CKM matrix and quark-mass independent divergences. This is in contrast with models possessing a direct ALP-quark coupling, in which the FCNC rate is sensitive to the UV completion [42, 52].

Table 1. The relevant parameters and input numbers.

parameters	input (GeV)	parameters	input numbers
m_Z	91	G_F	$1.1664\times10^{-5}\,\text{GeV}^{-2}$
m_W	80	s_W^2	0.23129
m_t	173	Γ_{B_s}	$65.81\times10^{10}\,s^{-1}$
m_b	4.183	Γ_{B^+}	$1/1638\times10^{15}\,s^{-1}$
m_c	1.2730	Γ_{B^0}	$1/1517\times10^{15}\,s^{-1}$
m_e	0.511×10^{-3}	Γ_{K^+}	$1/1.2380\times10^{8}\,s^{-1}$
m_μ	0.10566	Γ_K	$1/5.116\times10^{8}\,s^{-1}$
m_τ	1.777		
m_{B_s}	5.36693	$\sin\theta_{12}$	0.22501
m_{B^+}	5.27941	$\sin\theta_{13}$	0.003732
m_{B^0}	5.27972	$\sin\theta_{23}$	0.04183
m_{K^+}	0.493677	δ	1.147
m_{K_L}	0.497611		
m_{π^+}	0.13957	$f_K\sqrt{B_K}$	0.132GeV
m_{π^0}	0.1349768	$f_{B_d}\sqrt{B_d}$	225MeV
m_{ρ^0}	0.770	$f_{B_s}\sqrt{B_s}$	274 MeV
m_ϕ	1.020		

By further using the equation of motion, the above effective interaction for the on-shell fermions can be converted into

$$\mathcal{L}_{d_i\to d_j} = ig_{ad_id_j}a\bar{d}_j(m_{d_j}P_L - m_{d_i}P_R)d_i + \text{H.c.}. \tag{14}$$

This forms show that the main interactions should be RH chiral quark structures due to $m_{d_i} >> m_{d_j}$.

III. PHENOMENOLOGICAL ANALYSIS

The above flavor-changing quark interaction induced by a-W-W coupling contributes to different observables. In this part, we drive the experimental constraints on the coupling g_{aW} and ALP mass m_a, as well as discussing possible ALP explanations for experimental anomalies.

A. Meson FCNC decay

The above quark couplings $a-d_i-d_j$ will mediate flavor-changing neutral current (FCNC) rare decays of heavy-flavor mesons at the tree level. The rare meson decays into mono-energetic final state mesons and on-shell ALP, $M_1 \to M_2 a$, are the most sensitive probes of flavor-violating ALP couplings. This indicates that the relevant interactions are constrained by the corresponding physical processes as shown in Table 2.

We exclusively focus on the bounds derived on the flavor-changing ALP couplings. For estimating the transition matrix element of meson rare decays, we take B meson as example with the form factors as [74, 75]

$$\begin{aligned}\langle P(p)|\bar{q}b|B(p_B)\rangle &= \left(\frac{m_B^2-m_p^2}{m_b-m_q}\right)f_0^P(q^2),\\ \langle V(p)|\bar{q}\gamma_5 b|B(p_B)\rangle &= \frac{-i2m_V\epsilon^*\cdot q}{m_b+m_q}A_0(q^2),\end{aligned} \tag{15}$$

where P and V correspond to pseudo-scalar and vector state mesons, respectively. For $B\to K^* a$ decay, the K^* meson actually only have longitudinally polarization contribution since the ALP is a pseudoscalar particle. For the Kaon rare decays, we can estimate its amplitude under the vertor current conserved assumption [44]. Note that the matrix element for $K^0\to\pi^0 a$ is related to $K^\pm\to\pi^\pm a$ by isospin symmetry. Therefore, the matrix element for $K_L(K_S)$ mass eigenstate is obtained by taking the imaginary (real) part of $K^\pm\to\pi^\pm a$ matrix element [76]. Therefore the corresponding decays for B and K mesons are expressed by

$$\begin{aligned}\Gamma(B^+\to\pi^+ a) &= \frac{m_B^3}{64\pi}|g_{abd}|^2\left|f_0^{B\to\pi}(m_a^2)\right|^2\left(1-\frac{m_\pi^2}{m_B^2}\right)^2\\ &\quad\times\lambda^{1/2}\left(\frac{m_\pi}{m_B},\frac{m_a}{m_B}\right),\\ \Gamma\left(\bar{B}^0\to\pi^0 a\right) &= \frac{1}{2}\Gamma\left(B^-\to\pi^- a\right),\\ \Gamma(B\to Ka) &= \frac{m_B^3}{64\pi}|g_{abs}|^2\left(1-\frac{m_K^2}{m_B^2}\right)^2|f_0^{B\to K}(m_a^2)|^2\\ &\quad\times\lambda^{1/2}\left(\frac{m_K}{m_B},\frac{m_a}{m_B}\right),\\ \Gamma(B\to K^* a) &= \frac{m_B^3}{64\pi}|g_{abs}|^2|A_0(m_a^2)|^2\lambda^{3/2}\left(\frac{m_{K^*}}{m_B},\frac{m_a}{m_B}\right),\\ \Gamma(K^+\to\pi^+ a) &= \frac{m_{K^+}^3}{64\pi}\left(1-\frac{m_{\pi^+}^2}{m_{K^+}^2}\right)^2|g_{asd}|^2\\ &\quad\times\lambda^{1/2}\left(\frac{m_{\pi^+}}{m_{K^+}},\frac{m_a}{m_{K^+}}\right),\\ \Gamma(K_L\to\pi^0 a) &= \frac{m_{K_L}^3}{64\pi}\left(1-\frac{m_{\pi^0}^2}{m_{K_L}^2}\right)^2\text{Im}(g_{asd})^2\\ &\quad\times\lambda^{1/2}\left(\frac{m_{\pi^0}}{m_{K_L}},\frac{m_a}{m_{K_L}}\right),\end{aligned} \tag{16}$$

where $\lambda(x,y)=[1-(x+y)^2][1-(x-y)^2]$. Note that the factor $1/2$ in $\Gamma(\bar{B}^0\to\pi^0 a)$ comes from the quark components $\pi^0=(\bar{u}u+\bar{d}d)/\sqrt{2}$. The other decay processes can be obtained by the corresponding transformations on the masses and form factors. Using light-cone sum rules [74, 75], the corresponding expressions are

$$\begin{aligned}A_0^{B\to K^*}(m_a^2) &= \frac{1.364}{1-m_a^2/(5.28)^2}+\frac{-0.990}{1-m_a^2/36.78},\\ A_0^{B\to\rho}(m_a^2) &= \frac{1.527}{1-m_a^2/5.28^2}+\frac{-1.220}{1-m_a^2/33.36},\\ A_0^{B_s\to\phi}(m_a^2) &= \frac{3.310}{1-m_a^2/5.28^2}+\frac{-2.835}{1-m_a^2/31.57},\\ f_0^{B\to\pi}(m_a^2) &= \frac{0.258}{1-m_a^2/33.81},\\ f_0^{B\to K}(m_a^2) &= \frac{0.330}{1-m_a^2/37.46}.\end{aligned} \tag{17}$$

Note that the above forms fix the axion mass unit with m_a/GeV. In all cases these couplings are renormalized at the scale of the measurement, but because the flavor-changing ALP couplings do not run below the weak scale, it is equivalent to use couplings renormalized at the weak scale. Additionally, we expect that subprocesses of the type $B^-\to\pi^- a$ via ALP-pion mixing give rise to subdominant contributions to the $B^-\to\pi^-$ rate. The assumtions can be applied into other meson decays.

We should stress that the NP effects in the K^+ and in the K_L decay are in general highly correlated by the Grossman-Nir bound [77] with

Table 2. The SM predictions and the experimental measurements of the meson decays. Upper limits are all given at 90% confidence level (CL). Note that the symbol $*$ means the contribution is obtained by subtracting the tree-level effect from $B^+ \to \tau^+(\to K^{*+}\bar{\nu})\nu$, $[(10.86 \pm 1.43) - (1.07 \pm 0.10)] \times 10^{-6}$.

quark transition	Observable	SM prediction ($\times 10^{-6}$)	Experimental data ($\times 10^{-6}$)
$s \to d$	$Br(K^+ \to \pi^+ \nu\bar{\nu})$	$(8.42 \pm 0.61) \times 10^{-5}$ [53]	$(13.0^{+3.3}_{-3.0}) \times 10^{-5}$(NA62 [39, 40])
	$Br(K_L \to \pi^0 \nu\bar{\nu})$	$(3.41 \pm 0.45) \times 10^{-5}$ [53]	$< 3 \times 10^{-3}$(KOTO [54])
	$Br(K^+ \to \pi^+ ee)$	0.3 ± 0.03 [55]	0.3 ± 0.009(NA48 [37])
	$Br(K^+ \to \pi^+ \mu\mu)$	$(9.4 \pm 0.6) \times 10^{-2}$ [55]	$(9.17 \pm 0.14) \times 10^{-2}$(NA62 [37])
	$Br(K_L \to \pi^0 ee)$	$(3.38 \pm 0.92) \times 10^{-5}$ [56]	$< 2.8 \times 10^{-4}$(KTEV [57])
	$Br(K_L \to \pi^0 \mu\mu)$	$(1.39 \pm 0.27) \times 10^{-5}$ [56]	$< 3.8 \times 10^{-4}$(KTEV [58])
$b \to d$	$Br(B^+ \to \pi^+ \nu\bar{\nu})$	0.140 ± 0.018 [53]	< 14(Belle II [59])
	$Br(B^0 \to \pi^0 \nu\bar{\nu})$	0.0652 ± 0.0085 [53]	< 9(Belle II [59])
	$Br(B^+ \to \rho^+ \nu\bar{\nu})$	0.406 ± 0.079 [53]	< 30(Belle II [59])
	$Br(B^0 \to \rho^0 \nu\bar{\nu})$	0.189 ± 0.036 [53]	< 40(Belle II [59])
	$Br(B^+ \to \pi^+ ee)$	$(1.95 \pm 0.61) \times 10^{-2}$ [60]	$< 5.4 \times 10^{-2}$(Belle-II [61])
	$Br(B^0 \to \pi^0 ee)$	$(0.91 \pm 0.34) \times 10^{-2}$ [60]	$< 7.9 \times 10^{-2}$(Belle-II [61])
	$Br(B^+ \to \rho^+ ee)$	O(0.02) [37]	< 0.467(Belle-II [61])
	$Br(B^+ \to \pi^+ \mu\mu)$	$(1.95 \pm 0.61) \times 10^{-2}$ [60]	$(1.78 \pm 0.23) \times 10^{-2}$(LHCb [37])
	$Br(B^0 \to \pi^0 \mu\mu)$	$(0.91 \pm 0.34) \times 10^{-2}$ [60]	$< 5.9 \times 10^{-2}$(Belle-II [61])
	$Br(B^+ \to \rho^+ \mu\mu)$	O(0.02) [37]	< 0.381(Belle II [61])
	$Br(B \to \mu\mu)$	$(1.03 \pm 0.05) \times 10^{-4}$ [62]	$< 1.5 \times 10^{-4}$(CMS [63])
	$Br(B \to \tau\tau)$	0.03 [64]	< 2100(CMS [63])
$b \to s$	$Br(B^+ \to K^+ \nu\bar{\nu})$	(4.97 ± 0.37) (HPQCD[65])	$23 \pm 5^{+5}_{-4}$(Belle II [38])
	$Br(B^0 \to K^0 \nu\bar{\nu})$	3.85 ± 0.52 [53]	< 26(Belle [66])
	$Br(B^+ \to K^{*+} \nu\bar{\nu})$	$9.79 \pm 1.43^*$ [67]	< 61(Belle [66])
	$Br(B^0 \to K^{*0} \nu\bar{\nu})$	9.05 ± 1.37 [67]	< 18(Belle [66])
	$Br(B_s \to \phi \nu\bar{\nu})$	9.93 ± 0.72 [53]	< 5400(LEP DELPHI [68])
	$Br(B^+ \to K^+ ee)$	0.191 ± 0.015 [56]	0.56 ± 0.06(Belle [37])
	$Br(B^0 \to K^0 ee)$	0.51 ± 0.16 [60]	0.25 ± 0.11(Belle [37])
	$Br(B \to K^* ee)$	0.239 ± 0.028 [56]	1.42 ± 0.49(Belle-II [69])
	$Br(B^+ \to K^+ \mu\mu)$	0.191 ± 0.015 [56]	0.1242 ± 0.0068(CMS [70])
	$Br(B^0 \to K^0 \mu\mu)$	0.51 ± 0.16 [60]	0.339 ± 0.035(Belle [37])
	$Br(B \to K^* \mu\mu)$	0.239 ± 0.028 [56]	1.19 ± 0.32(Belle-II [69])
	$Br(B_s \to \phi \mu\mu)$	(0.27 ± 0.025) [56]	0.814 ± 0.047(LHCb [71])
	$Br(B^+ \to K^+ \tau\tau)$	0.12 ± 0.032 [60]	< 2250(BaBar [72])
	$Br(B_s \to \mu\mu)$	$(3.78 \pm 0.15) \times 10^{-3}$ [56]	$(3.34 \pm 0.27) \times 10^{-3}$(CMS [63])
	$Br(B_s \to \tau\tau)$	0.8 [64]	< 6800(LHCb [73])

$$\frac{\mathrm{BR}(K_L \to \pi^0 \nu\bar{\nu})}{\mathrm{BR}(K^+ \to \pi^+ \nu\bar{\nu})} < 4.3\,. \tag{18}$$

B. semi- and pure- leptonic meson decays

Although ALPs do not interact with fermions at the UV scale, the one-loop RG evolution from the UV scale Λ down to the weak scale induces the flavor conserving coupling to fermions $\mathcal{L} \supset g_{aFF} \partial_\mu a \bar{F} \gamma^\mu \gamma^5 F$ [51] as

$$g_{aFF} = \frac{3\alpha^2}{4}\left[\frac{3}{4s_W^4}\frac{g_{aW}}{g^2} + \frac{(Y_{F_L}^2 + Y_{F_R}^2)}{c_W^4}\frac{g_{aB}}{g'^2}\right]\log\frac{\Lambda^2}{m_W^2} + \frac{3}{2}Q_F^2\frac{\alpha}{4\pi}g_{a\gamma\gamma}\log\frac{m_W^2}{m_F^2}\,, \tag{19}$$

where $Y_{F_{L,R}}$ are the hypercharges of the chiral fermion F fields, and $s_W = \sin\theta_W$ and $c_W = \cos\theta_W$. In our study, we choose $\Lambda = 10\text{TeV}$.

The above forms $g_{a\gamma\gamma}$ in Eq. (4) comes from the tree level contribution. The loop corrections also contributes to the coupling given by

$$\frac{g^{loop}_{a\gamma\gamma}}{e^2} = \frac{g_{aW}}{2\pi^2} B_2\left(\frac{4m_W^2}{m_a^2}\right) - \sum_F \frac{N_c^F Q_F^2}{2\pi^2} g_{aFF} B_1\left(\frac{4m_F^2}{m_a^2}\right), \quad (20)$$

with the form of the functions as

$$B_1(x) = 1 - xg(x)^2, \quad B_2(x) = 1 - (x-1)g(x)^2,$$
$$g(x) = \begin{cases} \arcsin\dfrac{1}{\sqrt{x}} & \text{for} \quad x \geq 1 \\ \dfrac{\pi}{2} + \dfrac{i}{2}\log\dfrac{1+\sqrt{1-x}}{1-\sqrt{1-x}}, & \text{for} \quad x < 1. \end{cases} \quad (21)$$

where $N_c^F = 1(3)$ stands for the charged leptons (quarks). Therefore, the total ALP couplings with photons should consider the tree and loop level contributions simultaneously, $g^{eff}_{a\gamma\gamma} = g_{a\gamma\gamma} + g^{loop}_{a\gamma\gamma}$.

Correspondingly, the decay widths are obtained by

$$\Gamma_{total} = \sum_F \Gamma(a \to F\bar{F}) + \Gamma(a \to \text{hadrons}) + \Gamma(a \to \gamma\gamma),$$
$$\Gamma(a \to F\bar{F}) = \frac{N_c^F}{2\pi} m_a m_F^2 g_{aFF}^2 \left(1 - \frac{4m_F^2}{m_a^2}\right)^{1/2}, \quad (22)$$

$$\Gamma(a \to \text{hadrons}) = \frac{1}{8\pi^3}\alpha_s^2 m_a^3 \left(1 + \frac{83}{4}\frac{\alpha_s}{\pi}\right)\left|\sum_{q=u,d,s} g_{aqq}\right|^2,$$
$$\Gamma(a \to \pi^a\pi^b\pi^0) = \frac{\pi}{24}\frac{m_a m_\pi^4}{f_\pi^2}\left[\frac{g_{auu} - g_{add}}{32\pi^2}\right]^2 g_{ab}\left(\frac{m_\pi^2}{m_a^2}\right),$$
$$\Gamma(a \to \gamma\gamma) = \frac{m_a^3}{64\pi}|g^{eff}_{a\gamma\gamma}|^2, \quad (23)$$

where the fermion F stands for the charged leptons e,μ,τ and heavy quarks c,b,t. Note that the decay channel $a \to 3\pi$ only applies for $m_a > 3m_\pi$. The ALP decay into three pion final states can be derived using the effective chiral Lagrangian, in which the degrees of freedom associated with light quark masses are integrated out. Therefore these decay widths are not affected by the light quark mass. And $f_\pi = 0.13\text{GeV}$ means the pion meson decay constant. For $m_a > 1\text{GeV}$, the $a \to 3\pi$ channel will be absorbed into the $a \to$ hadrons one. And the corresponding functions are defined by

$$g_{00}(r) = \frac{2}{(1-r)^2}\int_{4r}^{(1-\sqrt{r})^2} dz \sqrt{1 - \frac{4r}{z}}\lambda^{1/2}(\sqrt{z}, \sqrt{r}),$$
$$g_{+-}(r) = \frac{12}{(1-r)^2}\int_{4r}^{(1-\sqrt{r})^2} dz \sqrt{1 - \frac{4r}{z}} \times (z-r)^2\lambda^{1/2}(\sqrt{z}, \sqrt{r}). \quad (24)$$

Furthermore, the branching ratios for the corresponding decay chains can be determined. Notably, the total decay width Γ_{total} plays a critical role in determining whether the ALP decays within the experimental detector.

If ALP can decay into the above SM particles within the length of detector, we should consider the ALP decay probability defined as

$$\mathcal{P}^a_{\text{dec}} = 1 - \exp\left(-\ell_D \Gamma_a \frac{M_a}{p_a}\right), \quad (25)$$

where ℓ_D refers to the transverse radius size of the detector, with 2.5 meters for NA62 and KOTO, 1.5 meters for BaBar, 1.8 meters for NA48, 1 meter for KTeV, 2 (4) meters for Belle (Belle-II), 7.5 meters for CMS, 6 meters for LEP, and 5 meters for LHCb, respectively.

Therefore, the branching ratios of the subsequent semi-leptonic decays are

$$Br(M_1 \to M_2 ll) = Br(M_1 \to M_2 a)Br(a \to ll)\mathcal{P}^a_{\text{dec}}. \quad (26)$$

The experimental data can constrain the model parameters for the decay $a \to ll$ if it occurs kinematically, $m_a > 2m_l$.

In addition to the aforementioned semi-leptonic decays, pure leptonic decays can serve as sensitive probes of flavor-changing ALP couplings. Properly accounting for their interference, we find that the ALP contribution modifies the branching ratios [9]

$$R(B_{s,d}) = \frac{\text{Br}(B_{s,d} \to ll)}{\text{Br}(B_{s,d} \to ll)_{\text{SM}}} = \left|1 - \frac{g_{all}}{C_{10}^{\text{SM}}(\mu_b)}\frac{\pi}{\alpha(\mu_b)}\frac{v_{SM}^2}{1 - m_a^2/m_{B_{s,d}}^2}\frac{g_{abs,abd}}{V_{ts}^* V_{tb}}\right|^2, \quad (27)$$

where $C_{10}^{SM}(m_b) \approx -4.2$ means the wilson coefficient of the operator $O_{10} = \bar{s}_L\gamma_\mu b_L \bar{\ell}\gamma^\mu\gamma_5\ell$ [78]. We choose the strongest bounds from muons as shown in Table 2.

C. Neutral-meson mixing

The meson mixing $\Delta F = 2$ can also place bounds on the model parameters. Neutral meson mixing is governed by the off-diagonal entries of the two-state Hamiltonian

$\hat{H} = \hat{M} - i\hat{\Gamma}/2$, where the Hermitian 2×2 matrices $\hat{M}$ and $\hat{\Gamma}$ describe the off-shell and on-shell transitions respectively. The effective Hamiltonian $H^{ij}_{\Delta F=2}$ receives contributions from both the SM and NP effects, with mixing amplitude defined as

$$\begin{aligned}\mathcal{L}_{\rm eff} = \bar{q}_1\Gamma_1 q_2 \bar{q}_1\Gamma_2 q_2 \quad &\Rightarrow \quad M_{12} = \frac{1}{2m_P}\langle\bar{P}|\mathcal{H}_{\rm eff}|P\rangle \\ &= -\frac{1}{2m_P}\langle\bar{P}|\bar{q}_1\Gamma_1 q_2 \bar{q}_1\Gamma_2 q_2|P\rangle\,, \end{aligned} \tag{28}$$

where $q_{1,2} = ds, db, sb$ correspond to the mixing of $K^0-\bar{K}^0$, $B_d-\bar{B}_d$ and $B_s-\bar{B}_s$, respectively. And $\Gamma_{1,2}$ means the different interaction structure combination. When considering the specific meson-mixing system, the mass differences for the K, B_d, B_s are

$$\Delta m_K = 2\Re(M^K_{12}),\ \Delta m_{B_q} = 2|M^{ib}_{12}|\,. \tag{29}$$

Note that for $K-\bar{K}$ mixing system, we need modify the absolute value as the real part.

The hadronic matrix elements of the relevant operators can then be written in terms of hadronic parameters $B_P(\mu)$ as

$$\frac{1}{m_P}\langle\bar{P}|\bar{q}_1\Gamma_1 q_2 \bar{q}_1\Gamma_2 q_2|P\rangle = f_P^2 m_P \eta(\mu) B_P(\mu)\,, \tag{30}$$

where the decay constant of f_P meson and the bag parameter B_P can refer to Refs. [79, 80] with numbers shown in Table 1. The meson $P(H\bar{q})$ is composed of one heavy quark H and one light antiquark $\bar{q}$.

For the above interaction in Eq. (12), it can naturally lead to the four-fermion operators. Adopting the notations in Ref. [81], the relevant two effector operators are expressed in the following

$$\begin{aligned}&\mathcal{H}_{eff} = \tilde{c}_2(\mu_H)\tilde{O}_2 + \tilde{c}_3(\mu_H)\tilde{O}_3, \\ &\tilde{O}_2 = \bar{q}^\alpha_L H^\alpha_R \bar{q}^\beta_L H^\beta_R\,, \quad \tilde{O}_3 = \bar{q}^\alpha_L H^\beta_R \bar{q}^\beta_L H^\alpha_R\,. \end{aligned} \tag{31}$$

For the case of $m_a \le m_b$, the wilson coefficients are

$$\begin{aligned}\tilde{c}_2(\mu_H) &= -\frac{m_H^2(\mu_H)}{2}\frac{N_c^2 A_+ - A_-}{(N_c^2-1)} g^2_{ad_id_j}\,, \\ \tilde{c}_3(\mu_H) &= -\frac{m_H^2(\mu_H)}{2}\frac{N_c (A_- - A_+)}{(N_c^2-1)} g^2_{ad_id_j}\,, \end{aligned} \tag{32}$$

where $A_\pm = 1/[(m_H \pm (m_P - m_H))^2 - m_a^2]$, and $N_c = 3$ means the color numbers for quarks. The superscripts α,β mean the corresponding color indices. The normalization factors $\eta(\mu)$ are conventionally obtained using the naive vacuum insertion (VIA) approximation for the matrix elements. Under the VIA condition, the above two operators $\tilde{O}_{2,3}$ will lead to $\eta(\mu)$ as

$$\begin{aligned}\tilde{\eta}_2(\mu_H) &= -\frac{1}{2}\left(1-\frac{1}{2N_c}\right)\left(\frac{m_P}{m_H+m_q}\right)^2\,, \\ \tilde{\eta}_3(\mu_H) &= -\frac{1}{2}\left(\frac{1}{N_c}-\frac{1}{2}\right)\left(\frac{m_P}{m_H+m_q}\right)^2\,. \end{aligned} \tag{33}$$

For the case $m_a > m_H$, the relevant Wilson coefficients are replaced by

$$\begin{aligned}&\tilde{c}_2(\mu_b) = \left(0.983\eta^{-2.42} + 0.017\eta^{2.75}\right)\tilde{c}_2(\mu_a), \\ &\tilde{c}_2(\mu_a) = \frac{m_b^2(\mu_a)}{2m_a^2}\left(g_{ad_id_j}\right)^2, \eta = [\alpha_s(\mu_a)/\alpha_s(\mu_b)]^{6/23}\,, \end{aligned} \tag{34}$$

where we consider the running effects from axion mass scale down to the scale m_b.

These off-diagonal matrix elements are directly related to the experimentally measured quantities as shown in Table 3. We found that the SM predictions on Δm_F are consistent with experimental data within errors and the uncertainties from theoretical non-perturbative QCD effects are larger than those of data.

The mass differences for the neutral meson mixing system are

$$\Delta m_P = |\Delta m_P^{SM} - f_P^2 m_P \sum_i \tilde{c}_i(m_H)\eta_i(m_H)B_P^i(m_H)|. \tag{35}$$

Therefore, the neutral meson mixing can provide the constraints for the ALP parameter regions

D. ALP-Z boson interaction

For ALP couplings with the electroweak gauge bosons, the relevant interaction can also be probed through precision measurements of the properties of Z bosons.

Firstly, we focus on the exotic Z-boson decay $Z\to\gamma a$ induced by Eq. (4) at tree level. The decay rate can be obtained as

$$\Gamma(Z\to\gamma a) = \frac{m_Z^3}{384\pi} g^2_{a\gamma Z}\left(1-\frac{m_a^2}{m_Z^2}\right)^3\,. \tag{36}$$

Provided the Z boson total decay width $\Gamma_Z = 2.4955$GeV [37], we obtain the branching ratios as

$$Br(Z\to\gamma a) = 2\times10^{-3}\left(\frac{g_{a\gamma Z}}{2.8\times10^{-3}}\right)^2\left(1-\frac{m_a^2}{m_Z^2}\right)^3\,. \tag{37}$$

At 95% CL, the decay can be constrained by Z total decay width, which can be converted into $Br(Z\to inv) < 2\times10^{-3}$, which can constrain the corres-

Table 3. The SM prediction and experimental values of mass differences Δm_F for $\Delta F = 2$ mixing.

Mixing modes	SM prediction	Experimental data
$K-\bar{K}$	4.7 ± 1.8 (ns)$^{-1}$ [82]	5.293 ± 0.009(ns)$^{-1}$(PDG [37])
$B_d-\bar{B}_d$	$0.547^{+0.035}_{-0.046}$(ps)$^{-1}$ [83]	0.5065 ± 0.0019(ps)$^{-1}$(PDG [37])
$B_s-\bar{B}_s$	18.23 ± 0.63(ps)$^{-1}$ [83, 84]	17.765 ± 0.006(ps)$^{-1}$(PDG [37])

ponding model parameters, m_a and g_{aW}. The most stringent constraints arise from the L3 search in e^+e^- collisions at the Z resonance at LEP, where $\mathrm{Br}(Z\to\gamma a)<1.1\times10^{-6}$ [85], for photon energies exceeding 31 GeV.

Furthermore, ALP can have the subsequent decays $a\to\gamma\gamma, l^+l^-$, which produces the decay chains [86, 87]

$$\begin{aligned}
&Br(Z\to\gamma ee)<5.2\times10^{-4}\ (OPAL),\\
&Br(Z\to\gamma\mu\mu)<5.6\times10^{-4}\ (OPAL),\\
&Br(Z\to\gamma\tau\tau)<7.3\times10^{-4}\ (OPAL),\\
&Br(Z\to\gamma\gamma\gamma)<2.2\times10^{-6}\ (ATLAS).
\end{aligned}\tag{38}$$

These processes can place the constraints for the model parameters if kinematically allowed.

Additionally, the ALP couplings can affect electroweak precision observables at the loop level. The loop corrections can in general be described in terms of the usual oblique parameters S,T,U [88], with the forms as [89]

$$\begin{aligned}
S&=\frac{c_W^2s_W^2}{72\pi^2m_Z^2}g_{aW}g_{aB}\left[F(m_Z^2;a,\gamma)-F(m_Z^2;a,Z)\right],\\
U&=\frac{s_W^4g_{aW}^2}{72\pi^2m_Z^2}\\
&\quad\times\left[F(m_Z^2;a,\gamma)+\frac{c_W^2}{s_W^2}F(m_Z^2;a,Z)-\frac{1}{s_W^2c_W^2}F(m_W^2;a,W)\right].
\end{aligned}\tag{39}$$

with the function $F(k^2;a,V)$ defined as

$$\begin{aligned}
&3k^4\lambda(m_a/k,m_V/k)\times\left[B_0(k^2;m_a,m_V)-B_0(0;m_a,m_V)\right]\\
&-3k^2\left[(2m_a^2+2m_V^2-k^2)B_0(0;m_a,m_V)\right]\\
&-3k^2\left[A_0(m_a)+A_0(m_V)\right]+7k^2(3m_a^2+3m_V^2-k^2),
\end{aligned}\tag{40}$$

where the $A_0(m_0), B_0(p^2;m_0,m_1)$ means Passarino-Veltman functions denoted explicitly as

$$\begin{aligned}
A_0(m_0)&=m_0^2\left(1-\ln\frac{m_0^2}{\Lambda^2}\right),\\
B_0(p^2;m_0,m_1)&=\int_0^1\mathrm{d}x\times\ln\left[\frac{\Lambda^2}{xm_0^2+(1-x)m_1^2-x(1-x)p^2}\right].
\end{aligned}\tag{41}$$

The current global fits for the oblique parameters are $S=-0.04\pm0.10$, $T=0.01\pm0.12$ and $U=-0.01\pm0.09$ [37]. We found that within 1σ errors, these parameters approaches zero. The new-physics scale Λ denotes the axion breaking scale. By setting $\Lambda=10$TeV, S and U give the the bound correspondingly.

In views of the couplings $g_{a\gamma Z}$ at the tree level, we can consider the production of a photon in association with an ALP in colliders. For the e^+e^- colliders, the production process proceeds via Z propogator in the s-channel with the differential cross section as

$$\begin{aligned}
\frac{d\sigma(e^+e^-\to\gamma a)}{d\cos\theta}&=\frac{1}{512\pi}\frac{\alpha^2(s)}{\alpha(m_Z)}s^2\left(1-\frac{m_a^2}{s}\right)^3(1+\cos^2\theta)\\
&\quad\times\left[|V(s)|^2+|A(s)|^2\right],
\end{aligned}\tag{42}$$

where $\sqrt{s}$ is the center-of-mass energy and θ denotes the scattering angle of the photon relative to the beam axis. Here we neglect the electron mass. ALP emission from the initial-state leptons vanishes due to the loop-suppressed $a-e-e$ interaction. The vector and axial-vector form factors are given by

$$\begin{aligned}
V(s)&=\frac{1-4s_W^2}{4s_Wc_W}\frac{g_{a\gamma Z}}{s-m_Z^2+im_Z\Gamma_Z}+\frac{2g_{a\gamma\gamma}}{s},\\
A(s)&=\frac{1}{4s_Wc_W}\frac{g_{a\gamma Z}}{s-m_Z^2+im_Z\Gamma_Z}.
\end{aligned}\tag{43}$$

Analyzing the vector coupling $V(s)$, the first term is suppressed by $1-4s_W^2$ so that we can reasonably ignore this term. Additionally, it could have enhanced effect when $s\sim m_Z^2$. Integrating out the angle θ, we can obtain the cross section

$$\begin{aligned}
\sigma(e^+e^-\to\gamma a)|_{s=m_Z^2}&=\frac{\alpha(s)}{24}\left(1-\frac{m_a^2}{s}\right)^3\\
&\quad\times\left[\frac{m_Z^2}{\Gamma_Z^2}\frac{g_{a\gamma Z}^2}{64c_W^2s_W^2}+(g_{a\gamma\gamma}^{eff})^2\right].
\end{aligned}\tag{44}$$

Note that the contribution in the case of Z pole receives an enhancement factor $m_Z^2/\Gamma_Z^2\approx1330$. It shows that using on-shell decays of narrow heavy SM particles into ALPs rather than the production of ALPs via an on-shell particle provides a much enhanced sensitivity to the $a\gamma Z$

coupling on the Z pole.

For the ALP in our case, Higgs boson can decays into Z bosons and ALPs, $h \to Za$ and $h \to aa$. However, the two decay processes are not induced by the Wilson coefficient C_{WW} and C_{BB} so that we do not consider the relevant processes.

IV. ALP PARAMETER BOUNDS

Because the ALP couplings with fermions and gauge bosons depend on g_{aW} and g_{aB} at the same time, this means that both couplings will affect the phenomenology described above. Therefore, we consider four different scenarios: the photophobic ALP, ALP with $g_{aB} = 0$, same sign ALP and ALP with $g_{aW} = 0$. The first one turns off $g_{a\gamma\gamma} = 0$ at tree-level by imposing the specific condition $g_{aB} = -g_{aW} \tan^2\theta_W$ to eliminate ALP-photon interaction, while the third one adopts the same sign $g_{aB} = g_{aW} \tan^2\theta_W$ to enhance ALP-photon interaction. The left two ones requires $g_{aW,aB} = 0$ directly.

In the following, we will analyze the current experimental bounds and future sensitivity for these four different scenarios, respectively.

A. Photophobic ALP scenario $g_{a\gamma\gamma} = 0$

For the photophobic ALP scenario, the ALP coupling with the photon at the tree level is eliminated by the following condition:

$$g_{aB} = -g_{aW} \tan^2\theta_W \longrightarrow g_{a\gamma\gamma} = 0,$$
$$g_{a\gamma Z} = 2\tan\theta_W g_{aW}\,. \tag{45}$$

In this case, the branching ratios for the corresponding decay chains can be determined, as shown in Fig. 2(a). Note that the total branching fraction sums to less than unity because we exclusively display the decay channels (charged leptons and photons) pertinent to our subsequent analysis.. Other decay channels (hadronic final states and heavy quarks c/b) contribute to the total decay width (see Eq. 22). Additionally, in the photophobic scenario, the absence of tree ALP-photon coupling prevents the photon channel from dominating, in marked contrast to non-photophobic cases (Fig. 2). We found that

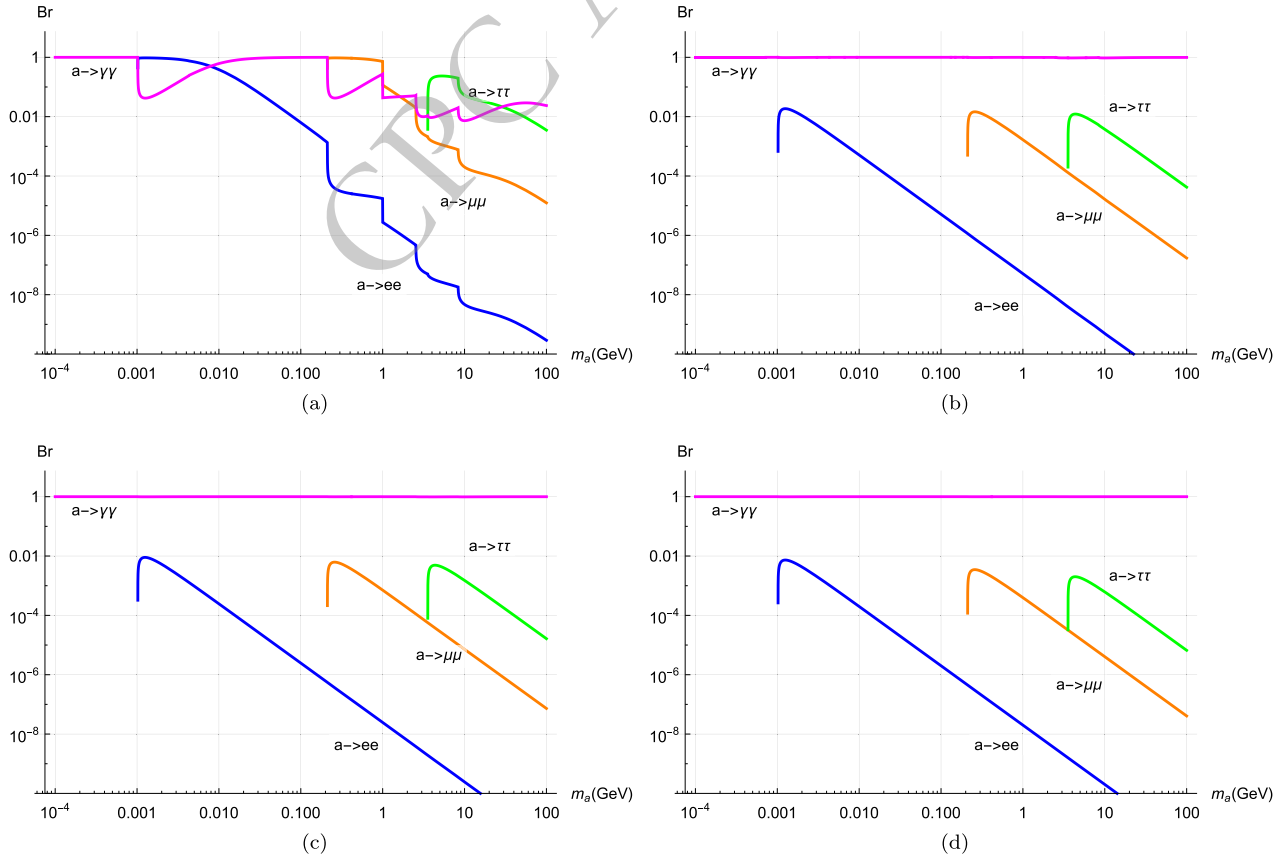

Fig. 2. (color online) The ALP branching ratios decays into different SM final states. The decays into photons, electrons, muons, and tauons are shown in magenta, blue, orange, and green, respectively. The upper left panel a) means the photobic ALP $g_{a\gamma\gamma} = 0$. The upper right panel b) means the ALP with $g_{aB} = 0$. The lower left panel c) means the same sign case $g_{aB} = g_{aW} \tan^2\theta_W$. The lower right panel d) means the ALP with $g_{aW} = 0$.

below $m_a < 2m_e$, the only decay channel is $a \to 2\gamma$. Additionally, the photon channels dominate the decay chains for $0.01 < m_a < 2m_\mu$ GeV and $m_a > 25$ GeV again, even if they are doubly suppressed by m_a^3. When the ALP mass approaches the double charged leptons, the dominant decay processes will convert into the corresponding leptons, with an order of magnitude proportional to the ALP mass m_a. Furthermore, the branching ratios into charged leptons (e,μ) decrease as the ALP mass increases, which significantly influences the shape of the parameter space contours. These indicate that the ALP subsequent decays $M_1 \to M_2 a(\to ll, 2\gamma)$ can provide constraints on the model parameters, as summarized in Table 2.

By inputting the photophobic form in Eq. (45) into the above phenomenological physical processes and comparing it to the experimental observables in Table 2, we can obtain the corresponding exclusion parameter regions for m_a and g_{aW}. The parameter bounds are plotted in Fig. 3(a). Here, we choose the ALP mass regions with $10^{-4} < m_a < 100$GeV. The lower bound indicates $m_a < 2m_e$, and the upper bound represents the electroweak scale.

We found that different physical processes exhibit distinctive exclusion abilities, as shown in different colors. For three different quark transitions, $s \to d$, $b \to d$, and $b \to s$, different decays demonstrate distinct exclusion capabilities. Note that the physical processes $M_1 \to M_2 \nu\bar{\nu}$ should include the decay factor $(1-\mathcal{P}^a_{\rm dec})$ to place the parameter constraints when ALP decays outside the detector.

For the $s \to d$ quark transition, the most stringent bound comes from $K^+ \to \pi^+ a$ with $g_{aW} > 10^{-5.4}$ GeV^{-1} in the mass region $m_a < m_{K^+} - m_{\pi^+}$, which is stronger than $K_L \to \pi^0 a$ by an order of magnitude. It indicates that the NA62 experiment provides a comparable exclusive limit to the previous E949 experiment. Note that the gap around $m_a \in (100, 150)$ MeV is due to the pion mass pole from the NA62 Collaboration [39]. Additionally, the GN bound provides stronger constraints, especially in the mass gap region and for large g_{aW} shown in the blue dashed line. It approaches $g_{aW} \sim 10^{-5}$ GeV^{-1}, providing much stronger constraints than $K_L \to \pi a$, but weaker constraints than $K^+ \to \pi^+ a$.

For $b \to d$ quark transition, $B \to \pi a$ provides the most stringent bounds with $g_{aW} < 10^{-3.3}$ GeV^{-1} for $m_a < 0.16$ GeV. Correspondingly, the bound weakens as follows: $B^+ \to \rho^+ a$ with $g_{aW} < 10^{-3.2}$ GeV^{-1}, $B_s \to \phi a$ with $g_{aW} < 10^{-3}$ GeV^{-1}, and $B^0 \to \rho a$ with $g_{aW} < 10^{-2.8}$ GeV^{-1}. Additionally, large couplings with $g_{aW} > 10^{-2.6}$ results in a loss of distinguishable capability for $b \to d$ processes.

For $b \to s$ quark transition, $B^0 \to K^{0*} a$ provides the most stringent bounds with $g_{aW} < 10^{-4.2}$ GeV^{-1} for $m_a < 4.5$ GeV. The limiting capability decreases sequentially by a factor of 1.6 from $B^0 \to K^{0*} a$, $B \to K a$, to $B^+ \to K^{+*} a$.

If $m_a > 2m_l$, the semi-leptonic decay $M_1 \to M_2 ll$ can occur kinematically. Therefore, the relevant decay processes can provide bounds on model parameters within reasonable regions in Fig. 3(a). For $M_1 \to M_2 ee$, the strongest bounds come from $K_L \to \pi ee$ within the oval for $0.001 < m_a < 0.1$ GeV. The following bounds are from $B \to K ee$, $B^+ \to \pi^+ ee$, $B^+ \to K^+ ee$, $K^+ \to \pi^+ ee$, $B^0 \to \pi^0$, and $B^+ \to \rho^+$ within their respective circles. For $M_1 \to M_2 \mu\mu$, $B^+ \to K^+ \mu\mu$ excludes $g_{aW} > 10^{-4.8}$ GeV^{-1}, followed by $B \to K\mu\mu$, $B^+ \to \pi^+ \mu\mu$, $B_s \to \phi\mu\mu$, $B \to K^* \mu\mu$, $B \to \pi\mu\mu$ and $B \to \rho\mu\mu$. Additionally, the upward-right tilt of the contour for $M_1 \to M_2 ll$ arises from the reduction in $Br(a \to ll)$, implying that larger values of the coupling g_{aW} are excluded by Eq. (26). These bounds effectively complement the unexplored regions for $K^+ \to \pi^+ a$, particularly in the range $2m_l < m_a < m_{M_1} - m_{M_2}$.

Moreover, the purely leptonic decays $B_{d/s} \to ll$ can provide bounds shown in brown. Currently, experimental data indicate that muon final states impose stronger constraints than tauon cases. Analyzing $B_{d/s} \to \mu\mu$, we find that $B_d \to \mu\mu$ provides significantly weaker bounds than $B_s \to \mu\mu$, around $10^{1.6}$ orders of magnitude, which constrains $g_{aW} < 10^{-1}$ GeV^{-1} at most mass ranges except $m_a \sim m_{B_s}$. Additionally, the excluded regions by $B_s \to \mu\mu$ fully encompass those by $B_d \to \mu\mu$.

Similarly, neutral meson mixings provide bounds shown in green. $B_s - \bar{B}_s$ mixing can place constraints across the ALP mass region with $g_{aW} < 10^{-1.4}$ GeV^{-1}. $B_d - \bar{B}_d$ mixing offers comparably weaker constraints. $K - \bar{K}$ mixing can achieve $g_{aW} \sim 10^{-2}$, which provides stronger bounds than $B_s - \bar{B}_s$ mixing, especially for $0.1 < m_a < 1$ GeV. Additionally, while neutral meson mixings provide weaker constraints compared to rare meson decays, they exclude some unexplored regions for meson decays.

For the Z boson properties, the bounds from Z boson decay chains are shown in yellow. Γ_Z excludes $g_{aW} > 10^{-2.8}$ GeV^{-1} across the ALP mass region. $Z \to a\gamma$ can reach $g_{aW} \sim 10^{-4.2}$ and fills a small region between the yellow line and rare meson decays. And the excluded region is fully covered by $M_1 \to M_2 ll$ for $m_a > 2m_\mu$. Similarly, ALP can decay into $\gamma\gamma, ll$ to produce $Z \to 3\gamma, \gamma ll$. The relevant bounds are shown in blue. $Z \to \gamma ee$, $Z \to \gamma\mu\mu$, and $Z \to \gamma\tau\tau$ exclude regions within their respective capabilities. And $Z \to 3\gamma$ provides the most stringent bounds, encompassing all $Z \to \gamma ee, \mu\mu$ regions and a significant portion of $Z \to \gamma\tau\tau$.

Besides, ultra-peripheral *Pb-Pb* collisions can produce ALPs through photon fusion, providing direct constraints on the ALP-photon coupling $g_{a\gamma\gamma}$ in the mass range $m_a = (5-100)$ GeV. These constraints are recast as a black solid line [90, 91]. We find that the bound from Pb-Pb collision is relatively weak and fully covered by other limits. Additionally, the Drell-Yan process $pp \to \gamma a$ at the LHC can provide bounds for $m_a > 100$ GeV, as

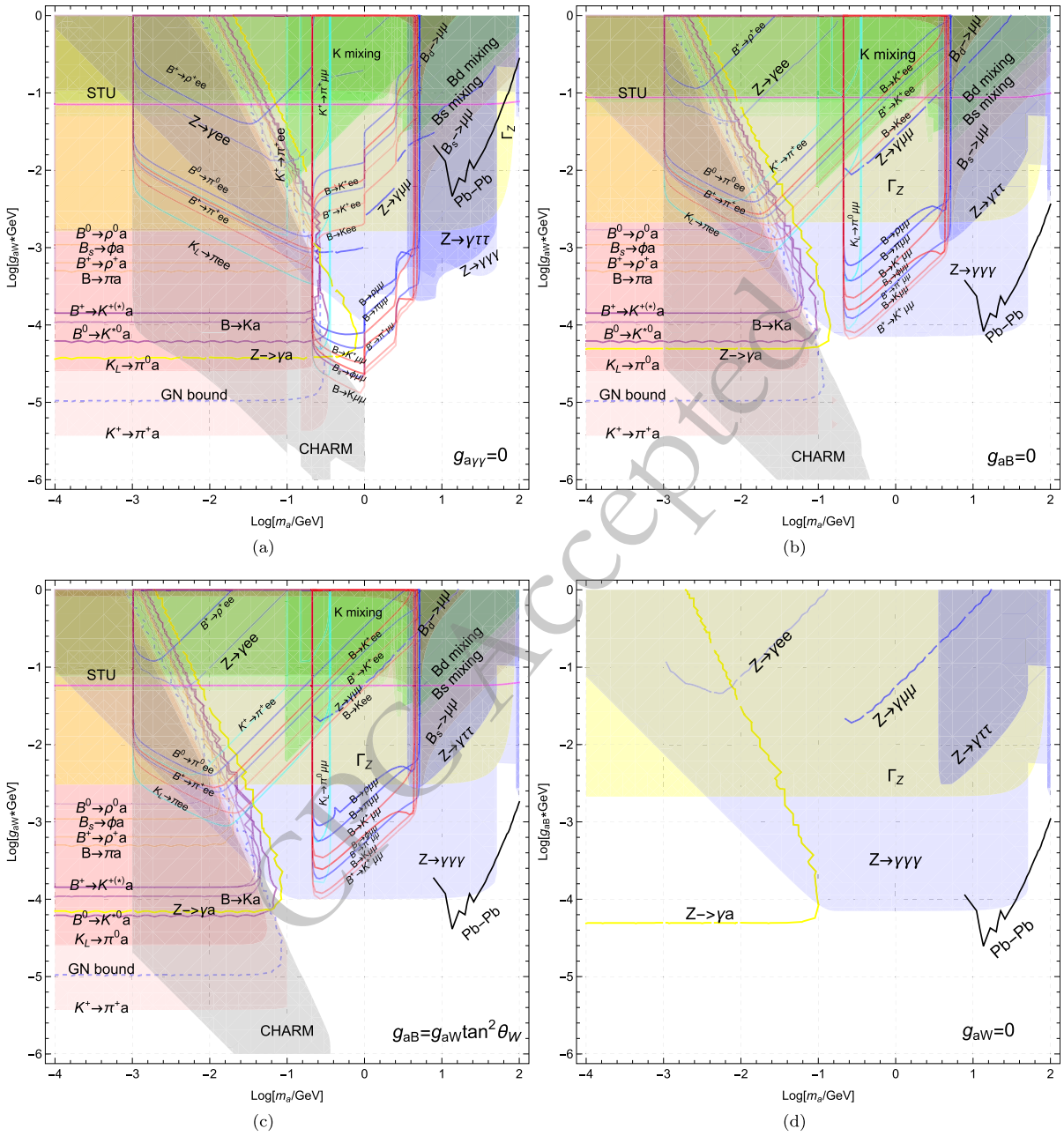

Fig. 3. (color online) The excluded parameter regions from different physical processes in the plane $m_a - g_{aW}$ or $m_a - g_{aB}$. The different physical processes exhibit distinctive exclusion capabilities, as shown in different colors. The upper left panel a) means the photobic ALP $g_{a\gamma\gamma} = 0$. The upper right panel b) means the ALP with $g_{aB} = 0$. The lower left panel c) means the same sign case $g_{aB} = g_{aW} \tan^2\theta_W$. The lower right panel d) means the ALP with $g_{aW} = 0$.

mentioned in Ref. [51], though this is beyond the mass range of interest in our study.

Proton beam dump experiments searching for long-lived particles provide constraints complementary to those from direct searches for rare meson decays. Production occurs through rare decays $K \to \pi a$ and $B \to \pi/Ka$, followed by the displaced decay $a \to \gamma\gamma, ee, \mu\mu$ within the detector. The strongest bound is from the CHARM experiment [92], with the number of signals from ALP decays estimated in [45, 93].

$$
\begin{aligned}
N_d \approx\ & 2.9\times 10^{17}\sigma\cdot \mathrm{Br}(a\to\gamma\gamma, ee, \mu\mu) \\
& \times\left[\exp\left(-\Gamma_a\frac{480\mathrm{m}}{\gamma}\right)-\exp\left(-\Gamma_a\frac{515\mathrm{m}}{\gamma}\right)\right], \\
\sigma =\ & \frac{3}{14}Br\left(K^+\to\pi^+ + a\right)+\frac{3}{28}Br\left(K_L\to\pi^0 + a\right) \\
& + 9\cdot 10^{-8} Br(B\to X + a)\ , \qquad (46)
\end{aligned}
$$

where $\gamma = 10\text{GeV}/m_a$. Since there is no signal from CHARM experiment, one then finds the 90% CL, $N_d < 2.3$ [93]. The corresponding region is shown in gray in Fig. 3(a). We observe that the CHARM experiment sets very strong bounds on the coupling g_{aW}. The CHARM shape exhibits three distinctive kick points, corresponding to the thresholds $2m_e$, $2m_\mu$ and 3π, respectively.

Therefore, we obtain the corresponding strongest bounds within the respective capability regions. These bounds are shown in gray in Fig. 5(a), respectively. In the following we want to analyze the future sensitivity for ALP parameter regions.

Firstly, we analyze the sensitivity of future lepton colliders for our model parameters. As indicated in Eq. (44), there is an enhancement factor m_Z^2/Γ_Z^2 particularly relevant for future colliders operating at the Z pole energy $\sqrt{s} = m_Z$. This highlights the importance of future lepton collider analyses at $\sqrt{s} = m_Z$. Fortunately, based on the conceptual design, two e^+e^- colliders with $\sqrt{s} = 91$ GeV exist: FCC-ee [94] and CEPC [95]. At this center-of-mass energy, the corresponding luminosities are 192 ab^{-1} and 16 ab^{-1}, respectively. This implies that the sensitivity of future lepton colliders can be employed to constrain the parameter space. The corresponding cross section is shown in Fig. 4(a). We found that for $g_{aW} \sim 10^{-2}$, the cross section approaches $\sigma(e^+e^- \to \gamma a) \sim (10^{-10} - 10^{-8})$ barn, depending on the ALP mass.

By further considering the decay of ALPs within the detector, we calculate the number of signal events as

$$N_{sig} = \sigma(e^+e^- \to \gamma a) \cdot \ell_{lum} (\mathcal{P}^a_{\text{dec}}(l_D) - \mathcal{P}^a_{\text{dec}}(r)), \tag{47}$$

where, ℓ_{lum} represents the luminosity of the lepton collider, and $r(l_D)$ denotes the minimal and maximal distances from the interaction point (IP) at which the detector can detect an ALP decay into SM particles. The main detector sensitivity is chosen as $r = 5$ mm and $l_D = 1.22$ mm [96], respectively. Requiring $N_{sig} \geq 3$, we obtain the future sensitivity shown as a dashed line in Fig. 5(a), for CEPC in magenta and FCC-ee in orange, respectively. We found that FCC-ee provides better sensitivity than CEPC. Furthermore, FCC-ee can even reach $g_{aW} \sim 10^{-7.4}$ GeV^{-1} for $m_a \sim 10^{1.6}$ GeV. Furthermore, the two colliders can cross check the bounds from $B \to K\mu\mu$. Additionally, the FCC-ee and CEPC lose their discriminative capabilities for $m_a > 10^{-0.8}$ GeV and $g_{aW} > 10^{-5}$GeV^{-1}.

The Search for Hidden Particles (SHiP) [97, 98] is an approved beam-dump experiment scheduled to begin operation in 2031. At SHiP, a 400 GeV proton beam extracted from the CERN SPS accelerator impacts a heavy proton target, resulting in significant production rates of pseudoscalar mesons K, B, B_s. These produced mesons can be utilized to search for ALPs through rare meson decays. Assuming a nominal operation of 15 years yields 6×10^{20} protons on target, SHIP can produce the total meson numbers 1.71×10^{20} for K, 8.1×10^{13} for $B^{0,\pm}$ and 2.16×10^{13} for B_s [99, 100], respectively. Assuming these mesons decay into ALPs within the detector, leading to observable signals, we can obtain

$$\begin{aligned} N_{sig} = &[N_K Br(K \to \pi a) + N_{B_s}(Br(B_s \to \phi a)) \\ &+ N_B \sum_i (Br(B \to M_i a)] \\ &\times \left[\exp\left(-\Gamma_a \frac{l}{\gamma}\right) - \exp\left(-\Gamma_a \frac{l+\Delta l}{\gamma}\right)\right], \end{aligned} \tag{48}$$

where $\gamma = 25\text{GeV}/m_a$, $i = \pi, K, K^*, \rho$ and their corresponding charged components are considered. Adopting the latest design [98], the detector HSDS is situated $l = 33$ m downstream from the target with decay volume $\Delta l = 50$m. Similarly, requiring $N_{sig} \geq 3$, we obtain the future projection shown as a green dashed line in Fig. 5(a). We find that SHiP provides significant sensitivity, particularly for small g_{aW}. Furthermore, the SHiP sensitivity projection completely encompasses the CHARM exclusion limits. Therefore, SHiP, CEPC and FCC-ee serve as complementary explorations for ALPs, focusing on distinct parameter regions.

Note that the above sensitivity analysis assumes a background-free environment based on the relatively clean experimental signatures. In practice, residual backgrounds including instrumental effects are expected, which would reduce the detection sensitivity. This leads to detection efficiency degradation, requiring enhanced couplings $g_{aW,aB}$. Consequently, the sensitivity regions shift upward. For simplicity, subsequent analysis focuses on the idealized background-free scenario.

B. ALP scenario with $g_{aB} = 0$

Another interesting scenario is the ALP with $g_{aB} = 0$, which couples only with $SU(2)_L$ gauge bosons as

$$g_{aB} = 0 \longrightarrow g_{a\gamma\gamma} = g_{aW} s_W^2,\ g_{a\gamma Z} = 2 c_W s_W g_{aW}. \tag{49}$$

Correspondingly, ALP interaction with fermions at loop level is obtained as

$$g_{aFF} = \frac{9\alpha g_{aW}}{64\pi s_W^2} \log\frac{\Lambda^2}{m_W^2} + \frac{3}{2} Q_F^2 \frac{\alpha}{4\pi} g_{a\gamma\gamma} \log\frac{m_W^2}{m_F^2}. \tag{50}$$

Note that the tree-level $g_{a\gamma\gamma}$ is significantly larger than the loop contribution $g^{loop}_{a\gamma\gamma}$ and g_{aFF}, by approximately one order of magnitude. The associated branching ratios for ALP decay processes are drawn in Fig. 2(b). We find that regardless of the ALP mass, the dominant decay channel is $a \to \gamma\gamma$ with a branching ratio close to 1. Addi-

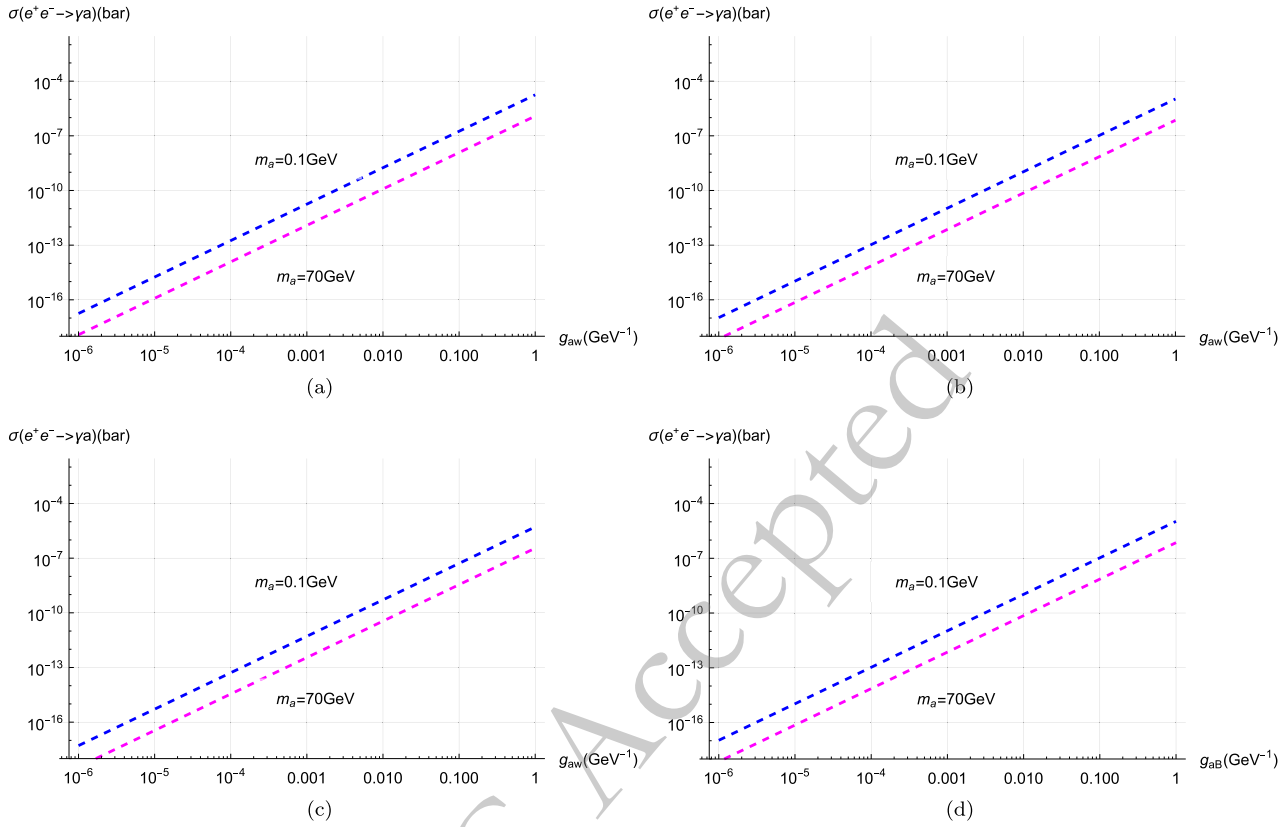

Fig. 4. (color online) The cross section of $e^+e^- \to \gamma a$ with the coupling $g_{aW}(\text{GeV}^{-1})$ in the center of mass energy $\sqrt{s} = m_Z$. Here we illustrate two ALP mass choice, $m_a = 0.5\text{GeV}$ and $m_a = 70\text{GeV}$. The upper left panel a) means the photobic ALP $g_{a\gamma\gamma} = 0$. The upper right panel b) means the ALP with $g_{aB} = 0$. The lower left panel c) means the same sign case $g_{aB} = g_{aW}\tan^2\theta_W$. The lower right panel d) means the ALP with $g_{aW} = 0$.

tionally, the chains decaying into charged leptons are strongly suppressed even if kinematically allowed. This feature differs significantly from the photophobic case. This suggests that different parameter bounds could exist in the ALP scenario with $g_{aB} = 0$.

Similarly, using Eq. (49) to analyze physical processes and comparing them with the experimental observables in Table 2, the corresponding exclusion parameter regions for g_{aW} are shown in Fig. 3(b) for $10^{-4} < m_a < 100$ GeV.

The different physical processes show distinct exclusion abilities represented by different colors. We find that the largest upper bound for g_{aW} maintains the same constraints as the photophobic ALP scenario. However, the corresponding excluded regions are narrowed due to the enhanced total decay width, affecting the decay factor $(1-\mathcal{P}^a_{\text{dec}})$.

For rare meson two-body decays $M_1 \to M_2 a$, three different quark transitions — $s \to d$, $b \to d$, and $b \to s$—will move left as the coupling g_{aW} increases. For instance, when $g_{aW} = 1$ GeV^{-1}, the excluded mass changes from $10^{-2.2}$ GeV in the photophobic scenario to 10^{-3} GeV. For the $s \to d$ quark transition, the lowest excluded value remains consistent with the photophobic case at $g_{aW} \sim 10^{-5.4}$ GeV^{-1}. Note that the original gap around the pion mass disappears approximately because the weakened exclusion capability constrains $m_a < 10^{-1}$ GeV. The excluded regions by the GN bound lie between $K_L \to \pi^0 a$ and $K^+ \to \pi^+ a$. Both reduce correspondingly to $m_a < 10^{-1}$ GeV. Similarly, the constrained ALP mass decreases from $10^{-0.6}$ GeV to 10^{-1} GeV for $b \to s$ quark transition, and from $10^{-0.8}$ GeV to $10^{-1.6}$ GeV for $b \to d$ quark transition. Correspondingly, the bound ability weakens similarly to the photophobic scenario, followed by $B \to \pi a$, $B^+ \to \rho^+ a$, $B_s \to \phi a$, and $B^0 \to \rho a$ for $b \to d$ transition. The limiting capability decreases sequentially from $B^0 \to K^{0*} a$, $B \to K a$ to $B^+ \to K^{+(*)} a$ for $b \to s$ transition. Additionally, the exclusion capability becomes indistinguishable for large coupling g_{aW}.

For the semi-leptonic decay $M_1 \to M_2 ll$, the constraints weaken when kinematically allowed decays occur. The bounded regions are illustrated in Fig. 3(b). For the electron case, the bounded circle shifts to the upper left panel, corresponding to $g_{aW} \sim 10^{-3}$, as given by $K_L \to \pi ee$. The subsequent bounds are derived from $B \to K ee$, $B \to K^* ee$, $B^+ \to K^+ ee$, $B^+ \to \pi^+ ee$, $B \to K^* ee$, $K^+ \to \pi^+ ee$, $B^0 \to \pi^0$, and $B^+ \to \rho^+$, each showing varying degrees of weakening. For muon cases, the correspond-

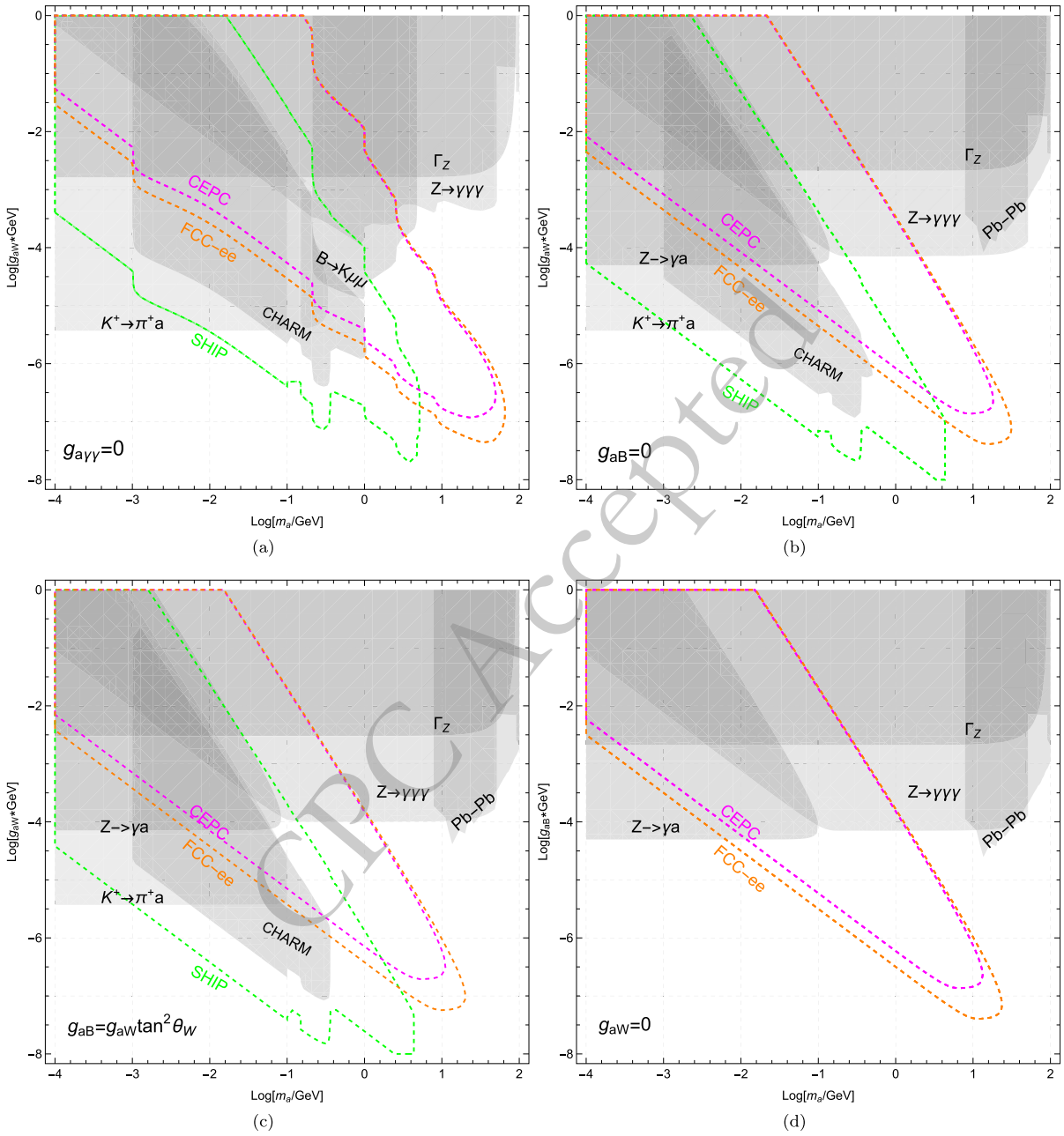

Fig. 5. (color online) The future sensitivity for ALP parameter in the plane $m_a - g_{aW}$ or $m_a - g_{aB}$. The future sensitivity of lepton colliders (CEPC,FCC-ee) and SHIP are based on background-free assumptions, represented by magneta, orange and green dashed lines, respectively. The upper left panel a) means the photobic ALP $g_{a\gamma\gamma} = 0$. The upper right panel b) means the ALP with $g_{aB} = 0$. The lower left panel c) means the same sign case $g_{aB} = g_{aW} \tan^2\theta_W$. The lower right panel d) means the ALP with $g_{aW} = 0$.

ing bounds shift upward, indicating that $M_1 \to M_2 ll$ impose weaker bounds on the model parameters, reduced by an order of magnitude of $10^{-0.6}$ compared to the photophobic case.

For the case of pure leptonic decays $B_{d/s} \to ll$, the bounds remain approximately the same in brown with the photophobic case due to minor modifications in g_{aFF}. $B_s \to \mu\mu$ excluded region fully encompasses the ones by $B_d \to \mu\mu$ with a decreased g_{aW}. Additionally, neutral meson mixings remain unchanged as the process solely depends on the coupling $g_{ad_id_j}$ induced by g_{aW}.

For the Z boson properties, the bounds from Z boson invisible decays increase slightly due to the modification $g_{a\gamma Z}$ from $2\tan\theta_W g_{aW}$ to $2c_W s_W g_{aW}$ as shown in yellow. Additionally, $Z \to a\gamma$ restricted interval decreases from $m_a \sim 10^{-0.2}$ GeV to $m_a \sim 10^{-0.8}$ GeV, indicating that the excluded regions do not intersect with $M_1 \to M_2\mu\mu$. This feature is obviously different from the photophobic scenario. This helps explore small regions in previously unexplored meson decays. Additionally, the exclusion capabil-

ity of $Z \to \gamma ll$ weakens to varying degrees. For instance, $Z \to \gamma\tau\tau$ constrains $g_{aW} < 10^{-2.8}$ GeV^{-1}, which is weaker than the previous bound $g_{aW} < 10^{-3.4}$ GeV^{-1} in the photophobic case. However, the enhanced decay ratio $a \to \gamma\gamma$ strengthens the corresponding bounds to around $g_{aW} < 10^{-4.2}$ GeV^{-1}, particularly for $m_a \in (10^{-1}, 10^{1.6})$ GeV. Furthermore, $Z \to 3\gamma$ covers all regions excluded by $Z \to \gamma ll$.

The Pb-Pb collision constraint is displayed as a black solid line. This provides the most stringent constraints in the ALP mass range $m_a = (91, 100)$ GeV.

Proton beam dump experiments (CHARM) have already excluded some regions in gray with a corresponding leftward shift. The excluded region by CHARM covers all coupling ranges $g_{aW} \in (10^{-6}, 1)$ GeV^{-1}. In the following, we analyze the future sensitivity for ALP parameter regions.

For the future lepton collider (CEPC, FCC-ee) operating at the Z pole with $\sqrt{s} = m_Z$, the corresponding cross section is shown in Fig. 4(b). We observe that the cross section only undergoes minor modifications. For example, $\sigma(e^+e^- \to \gamma a) \sim 10^{-7}$ bar for $m_a = 0.1$ GeV and $g_{aW} = 0.1$ GeV^{-1}.

After analyzing the ALP decay within the detector and requiring the signal events to be larger than 3, we obtain the future sensitivity shown as a dashed line in Fig. 5(b), for CEPC in magenta and FCC-ee in orange, respectively. FCC-ee can provide significantly better sensitivity than CEPC. On the other hand, SHiP can produce a large number of pseudoscalar mesons decaying into ALP with sensitivity shown in green dashed line. This indicates that SHiP can provide strong sensitivity, especially for small g_{aW}. This shows that they can serve as complementary explorations for ALP, focusing on different parameter regions, respectively.

C. Same sign ALP scenario $g_{aB} = g_{aW}\tan^2\theta_W$

Instead of selecting the opposite-sign coupling $g_{aB} = -g_{aW}\tan^2\theta_W$ to cancel out $g_{a\gamma\gamma}$ in the photophobic scenario,adopt the same-sign coupling $g_{aB} = g_{aW}\tan^2\theta_W$ to enhance $g_{a\gamma\gamma}$. We defined the case as same sign ALP scenario with

$$\begin{aligned} &g_{aB} = g_{aW}\tan^2\theta_W \longrightarrow g_{a\gamma\gamma} = 2g_{aW}s_W^2, \\ &g_{a\gamma Z} = 2\tan\theta_W g_{aW}(1-2s_W^2)\,. \end{aligned} \tag{51}$$

Correspondingly, ALP interaction with fermions at loop level is obtained as

$$\begin{aligned} g_{aFF} = &\frac{3\alpha}{16\pi}g_{aW}\left[\frac{3}{4s_W^2} + \frac{(Y_{F_L}^2 + Y_{F_R}^2)}{c_W^4}s_W^2\right]\log\frac{\Lambda^2}{m_W^2} \\ &+ \frac{3}{2}Q_F^2\frac{\alpha}{4\pi}g_{a\gamma\gamma}\log\frac{m_W^2}{m_F^2}\,. \end{aligned} \tag{52}$$

Note that the tree-level $g_{a\gamma\gamma}$ is four times larger compared the ALP scenario with $g_{aB} = 0$, and it is further significantly larger than both the loop contribution $g_{a\gamma\gamma}^{loop}$ and g_{aFF}. The associated branching ratios for ALP decay processes are drawn in Fig. 2(c), indicating that the dominant decay channel is $Br(a \to \gamma\gamma) \sim 1$ across the entire ALP mass range. Additionally, the decay into charged leptons is strongly suppressed, with ratios below 0.01. This feature is similar to the $g_{aB} = 0$ scenario, which yields similar parameter bounds.

Based on Eq. (51) to analyze physical processes and compare with the experimental observables in Table 2, the corresponding exclusion parameter regions for g_{aW} are shown in Fig. 3(c) for $10^{-4} < m_a < 100$ GeV.

The different physical processes show distinct exclusion abilities represented by different colors. We find that the bounds from meson decays, including $M_1 \to M_2 a$, $M_1 \to M_2 ll$ and $M_1 \to ll$, keep similar constraints to those in the ALP scenario with $g_{aB} = 0$. This is due to the loop-suppressed ALP couplings with fermions and photons, which results in $a \to \gamma\gamma$ being the dominant decay channel from the tree-level $g_{a\gamma\gamma}$.

Additionally, the other bounds maintain comparable exclusion capabilities, such as meson mixing and CHARM. The only significant changes involve Z boson-related processes. For the total decay width of the Z boson, the exclusion bound is modified to $g_{aW} < 10^{-2.6}$, improved from $g_{aW} < 10^{-2.8}$ in the $g_{aB} = 0$ scenarios as shown in yellow. Furthermore, $Z \to a\gamma$ restricted interval decreases from $m_a \sim 10^{-0.8}$ GeV to $m_a \sim 10^{-1.2}$ GeV, which adds to previously unexplored rare meson decays. Additionally, the exclusion capability of $Z \to \gamma ll$ weakens to varying degrees as shown in blue. For instance, $Z \to \gamma\tau\tau$ constrains $g_{aW} < 10^{-2.6}$ GeV^{-1}, which matches the exclusion capability of Γ_Z. Correspondingly, $a \to \gamma\gamma$ weakens the corresponding bounds to around $g_{aW} < 10^{-4}$ GeV^{-1} for $m_a \in (10^{0.4}, 10^{1.6})$ GeV. Furthermore, $Z \to 3\gamma$ covers all regions excluded by $Z \to \gamma ll$, even including the regions excluded by Γ_Z. This feature differs slightly from the $g_{aB} = 0$ scenario. Additionally, the bounds from Pb-Pb collisions in black line are particularly stringent for ALP masses in the range 10-100 GeV.

In the following, we analyze the future sensitivity for ALP parameter regions. For the future lepton collider (CEPC, FCC-ee) operating at the Z pole with $\sqrt{s} = m_Z$, the corresponding cross section is shown in Fig. 4(c), keeping the same cross section approximately.

Similarly, by analyzing the ALP decay within the detector and requiring the signal events to be greater than 3, we obtain the future sensitivity shown as a dashed line in Fig. 5(c), for CEPC in magenta and FCC-ee in orange. We find that the sensitivity shifts to the left, and the FCC-ee sensitivity can fully cover the CEPC sensitivity. On the other hand, SHiP sensitivity follows a similar trend of shifting to the left, providing strong sensitivity for small

$m_a < 4$ GeV.

D. ALP scenario with $g_{aW} = 0$

Correspondingly, another left ALP scenario is $g_{aW} = 0$, which only couples with $U(1)_B$ hypercharge gauge boson as

$$g_{aW} = 0 \longrightarrow g_{a\gamma\gamma} = g_{aB} c_W^2,$$
$$g_{a\gamma Z} = -2\cos\theta_W \sin\theta_W g_{aB}\,. \tag{53}$$

Similarly, ALP interaction with fermions at loop level is obtained as

$$g_{aFF} = \frac{3\alpha}{16\pi} g_{aB} \left[\frac{(Y_{F_L}^2 + Y_{F_R}^2)}{c_W^2}\right] \log\frac{\Lambda^2}{m_W^2} + \frac{3}{2} Q_F^2 \frac{\alpha}{4\pi} g_{a\gamma\gamma} \log\frac{m_W^2}{m_F^2}\,. \tag{54}$$

Note that the tree-level $g_{a\gamma\gamma}$ remains significantly larger than both the loop contribution $g_{a\gamma\gamma}^{loop}$ and g_{aFF}. The associated branching ratios for ALP decay processes are drawn in Fig. \ref{br_W}, demonstrating that the dominant decay channel is $Br(a \to \gamma\gamma) \sim 1$ across the entire ALP mass range. Furthermore, the decay branching ratios into charged leptons are significantly suppressed to below 0.01. This feature is consistent with other scenarios, which yield similar parameter constraints.

Based on Eq. (53) to analyze physical processes and compare with the experimental observables in Table 2, the corresponding exclusion parameter regions for g_{aW} are presented in Fig. 3(c) for $10^{-4} < m_a < 100$ GeV. Different physical processes exhibit distinct exclusion capabilities, represented by various colors. Note that for $g_{aW} = 0$, the flavor changing interactions in Eq. 12 vanish, causing the relevant bounds ($M_1 \to M_2 a$, $M_1 \to M_2 ll$ and meson mixings) to disappear. The only remaining physical processes are Z boson-related interactions. For $m_a < 0.1$GeV, the strongest bounds originate from $Br(Z \to \gamma a)$ with $g_{aB} < 10^{-4.3}\text{GeV}^{-1}$. For $m_a > 0.1$GeV, the stringent constraint arises from $Z \to 3\gamma$ with $g_{aB} < 10^{-4.2}\text{GeV}^{-1}$. Other subsequent decays, such as $Z \to all$, provide relatively weak constraints, which are entirely covered by the total decay width of the Z boson, Γ_Z, as indicated in yellow. Additionally, the Pb-Pb collision constraints in black solid line dominate over Z-boson decay limits across most of the parameter space for $m_a = (10, 100)$ GeV.

For the future sensitivity of ALP parameter regions, the projected performance of future lepton colliders (e.g., CEPC and FCC-ee) operating at the Z pole ($\sqrt{s} = m_Z$) is shown in Fig. 4(d). Similarly, by analyzing ALP decays within the detector and requiring at least three signal events, we derive the projected future sensitivity shown as dashed lines in Fig. 5(d), with CEPC in magenta and FCC-ee in orange. We find that FCC-ee offers significantly better sensitivity compared to CEPC. Additionally, they can act as complementary probes for ALPs, in comparison to Z boson decays.

V. CONCLUSION

We provide an updated and extended analysis on the experimental limits of the ALP couplings to electroweak gauge bosons across the ALP mass range from MeV to 100 GeV. In order to indicate the effects from two independent couplings (g_{aW} and g_{aB}), we analyze four distinct scenarios under various values of couplings. The couplings induce flavor-conserving ALP interactions with SM fermions at the one-loop level, while g_{aW} additionally gives rise to flavor-changing ALP-quark couplings within the framework of minimal flavor violation.

The relevant experimental constraints are illustrated in Fig. 3. We clearly depict the bounds from each different physical process. This helps us identify which process contributes to which specific constraint. For the three quark transition scenarios $s \to d$, $b \to d$, and $b \to s$, the strongest bounds are provided by $K^+ \to \pi^+ a$, $B \to \pi a$, and $B^0 \to K^{0*} a$, respectively. With more precise future measurements of certain processes, we will be able to understand how the constraints on the parameter space evolve. Comparing these four different scenarios ($g_{a\gamma\gamma} = 0$, $g_{aB} = 0$, $g_{aB} = g_{aW}\tan^2\theta_W$ and $g_{aW} = 0$), we find that the excluded region in the photophobic case is significantly weaker than in the other three cases due to the enhanced photon coupling at the tree level for the latter. The corresponding excluded regions shift to the left panel for these four scenarios along with the increased total ALP decay width. Another distinct difference is that the bounds from $M_1 \to M_2 ll$ move upper as the scenario transitions from photophobic and $g_{aB} = 0$ ALPs to same-sign ALPs, even vanish in the ALPs with $g_{aW} = 0$, indicating a gradual weakening of constraints. Furthermore, $Z \to 3\gamma$ in the last three scenario provides much stricter bounds than in the photophobic ALP case, owing to the enhanced branching ratio $a \to \gamma\gamma$. Additionally, Pb-Pb collisions provide stringent constraints in $m_a = (1, 100)$ GeV. Our finding highlights that rare meson decays, Z-boson decays, and Pb-Pb collisions provide complementary probes of ALP parameter space, covering MeV and GeV mass scales respectively.

The future experimental projections for ALP parameters are analyzed as shown in Fig. 5, including lepton colliders (CEPC, FCC-ee) and the Search for Hidden Particles (SHiP). For lepton colliders operating near the Z pole, the ALP production via $e^+e^- \to Z \to \gamma a$ experiences an enhancement factor of $m_Z^2/\Gamma_Z^2 = 1330$, requiring an analysis of the corresponding projection. We find that FCC-ee can provide better sensitivity than CEPC, allowing for

probing regions beyond the bounds from rare meson decays and Z boson decays. Moreover, SHiP can explore deeper into smaller g_{aW} values, fully surpassing the existing CHARM bounds. These indicate that future lepton colliders and SHiP can offer enhanced sensitivity for ALP parameters.

ACKNOWLEDGMENTS

We thank Prof. YuJi Shi and Prof. Sang Hui Im for useful discussion.

References

[1] R. D. Peccei and H. R. Quinn, Phys. Rev. Lett. **38**, 1440 (1977)
[2] S. Weinberg, Phys. Rev. Lett. **40**, 223 (1978)
[3] F. Wilczek, Phys. Rev. Lett. **40**, 279 (1978)
[4] H.-Y. Cheng, Phys. Rept. **158**, 1 (1988)
[5] J. E. Kim and G. Carosi, Rev. Mod. Phys. **82** (2010) 557–602, [arXiv:0807.3125].[Erratum: Rev.Mod.Phys. 91, 049902 (2019)].
[6] L. Di Luzio, M. Giannotti, E. Nardi, and L. Visinelli, Phys. Rept. **870**, 1 (2020), arXiv: 2003.01100
[7] M. Bauer, M. Neubert, and A. Thamm, JHEP **12**, 044 (2017), arXiv: 1708.00443
[8] K. Choi, S. H. Im, and C. Sub Shin, Ann. Rev. Nucl. Part. Sci. **71**, 225 (2021), arXiv: 2012.05029
[9] M. Bauer, M. Neubert, S. Renner, M. Schnubel, and A. Thamm, JHEP **09**, 056 (2022), arXiv: 2110.10698
[10] F. Arias-Aragón, J. Quevillon, and C. Smith, JHEP **03**, 134 (2023), arXiv: 2211.04489
[11] P. Sikivie, Phys. Rev. Lett. **51** (1983) 1415–1417.[Erratum: Phys.Rev.Lett. 52, 695 (1984)].
[12] H. Primakoff, Phys. Rev. **81**, 899 (1951)
[13] J. Jaeckel and A. Ringwald, Ann. Rev. Nucl. Part. Sci. **60**, 405 (2010), arXiv: 1002.0329
[14] A. Ringwald, *Review on Axions*, 4, 2024. arXiv: 2404.09036.
[15] J. Beacham, *et al*., J. Phys. G **47**(1), 010501 (2020), arXiv: 1901.09966
[16] L. Calibbi, Z. Huang, S. Qin, Y. Yang, and X. Yin, Phys. Rev. D **108**(1), 015002 (2023), arXiv: 2212.02818
[17] P. Rebello Teles, D. d'Enterria, V. P. Gonçalves, and D. E. Martins, Phys. Rev. D **109**(5), 055003 (2024), arXiv: 2310.17270
[18] **CAPP** Collaboration, S. Ahn *et al*., Phys. Rev. X **14** (2024), no. 3 031023, [arXiv: 2402.12892].
[19] A. Quiskamp, B. T. McAllister, P. Altin, E. N. Ivanov, M. Goryachev, and M. E. Tobar, Phys. Rev. Lett. **132**(3), 031601 (2024), arXiv: 2310.00904
[20] **ALPS** Collaboration, L.-W. Wei, PoS **TAUP2023** (2024) 049, [arXiv: 2401.14773].
[21] **CAST** Collaboration, K. Altenmüller *et al*., Phys. Rev. Lett. **133** (2024), no. 22 221005, [arXiv: 2406.16840].
[22] **NEON** Collaboration, B. J. Park *et al*., *Exploring the Cosmological Triangle in Search for Axion-Like Particles from a Reactor*, arXiv: 2406.06117.
[23] **HPQCD** Collaboration, C. Bouchard, G. P. Lepage, C. Monahan, H. Na, and J. Shigemitsu, Phys. Rev. D **88** (2013), no. 5 054509, [arXiv: 1306.2384]. [Erratum: Phys.Rev.D 88, 079901 (2013)].
[24] R. R. Horgan, Z. Liu, S. Meinel, and M. Wingate, Phys. Rev. D **89**(9), 094501 (2014), arXiv: 1310.3722
[25] A. J. Buras, J. Girrbach-Noe, C. Niehoff, and D. M. Straub, JHEP **02**, 184 (2015), arXiv: 1409.4557
[26] R. Alonso, B. Grinstein, and J. Martin Camalich, JHEP **10**, 184 (2015), arXiv: 1505.05164
[27] A. J. Buras, D. Buttazzo, J. Girrbach-Noe, and R. Knegjens, JHEP **11**, 033 (2015), arXiv: 1503.02693
[28] T. Blake, G. Lanfranchi, and D. M. Straub, Prog. Part. Nucl. Phys. **92**, 50 (2017), arXiv: 1606.00916
[29] J. Gao, C.-D. Lü, Y.-L. Shen, Y.-M. Wang, and Y.-B. Wei, Phys. Rev. D **101**(7), 074035 (2020), arXiv: 1907.11092
[30] W. Wang, F.-S. Yu, and Z.-X. Zhao, Phys. Rev. Lett. **125**(5), 051802 (2020), arXiv: 1909.13083
[31] M. Beneke, C. Bobeth, and Y.-M. Wang, JHEP **12**, 148 (2020), arXiv: 2008.12494
[32] Y.-K. Huang, Y.-L. Shen, C. Wang, and Y.-M. Wang, *Next-to-Leading-Order Weak Annihilation Correction to Rare $B\to K\{K,\pi\}\ell^+\ell^-$ Decays*, arXiv: 2403.11258.
[33] A. J. Buras, J. Harz, and M. A. Mojahed, JHEP **10**, 087 (2024), arXiv: 2405.06742
[34] M. Fedele, PoS **WIFAI2023** (2024) 022, [arXiv: 2402.03863].
[35] H.-J. Tian, H.-B. Fu, T. Zhong, Y.-X. Wang, and X.-G. Wu, *The rare decay $B^+\to K^+\ell^+\ell^-(\nu\nu)$ under the QCD sum rules approach*, arXiv: 2411.12141.
[36] T. Huber, T. Hurth, J. Jenkins, E. Lunghi, Q. Qin, and K. K. Vos, JHEP **11**, 130 (2024), arXiv: 2404.03517
[37] **Particle Data Group** Collaboration, S. Navas *et al*., Phys. Rev. D **110** (2024), no. 3 030001.
[38] **Belle-II** Collaboration, I. Adachi *et al*., Phys. Rev. D **109** (2024), no. 11 112006, [arXiv: 2311.14647].
[39] **NA62** Collaboration, E. Cortina Gil *et al*., JHEP **06** (2021) 093, [arXiv: 2103.15389].
[40] **NA62** Collaboration, E. Cortina Gil *et al*., *Observation of the $K^+\to\pi^+\nu\nu$ decay and measurement of its branching ratio*, arXiv: 2412.12015.
[41] **BNL-E949** Collaboration, A. V. Artamonov *et al*., Phys. Rev. D **79** (2009) 092004, [arXiv: 0903.0030].
[42] M. Freytsis, Z. Ligeti, and J. Thaler, Phys. Rev. D **81**, 034001 (2010), arXiv: 0911.5355
[43] A. Celis, J. Fuentes-Martin, and H. Serodio, Phys. Lett. B **741**, 117 (2015), arXiv: 1410.6217
[44] E. Izaguirre, T. Lin, and B. Shuve, Phys. Rev. Lett. **118**(11), 111802 (2017), arXiv: 1611.09355
[45] K. Choi, S. H. Im, C. B. Park, and S. Yun, JHEP **11**, 070 (2017), arXiv: 1708.00021
[46] J. Heeck, *Phenomenology of Majorons*, in 13th Patras Workshop on Axions, WIMPs and WISPs, pp. 212–215, 2018. arXiv: 1709.07670.
[47] J. Heeck and H. H. Patel, Phys. Rev. D **100**(9), 095015 (2019), arXiv: 1909.02029
[48] J. Martin Camalich, M. Pospelov, P. N. H. Vuong, R. Ziegler, and J. Zupan, Phys. Rev. D **102**(1), 015023 (2020), arXiv: 2002.04623
[49] Y. Cheng, C.-W. Chiang, X.-G. He, and J. Sun, Phys. Rev.

D **104**(1), 013001 (2021), arXiv: 2012.15287
[50] J. Sun, Y. Cheng, and X.-G. He, JHEP **04**, 141 (2021), arXiv: 2101.06055
[51] N. Craig, A. Hook, and S. Kasko, JHEP **09**, 028 (2018), arXiv: 1805.06538
[52] B. Batell, M. Pospelov, and A. Ritz, Phys. Rev. D **83**, 054005 (2011), arXiv: 0911.4938
[53] B.-F. Hou, X.-Q. Li, M. Shen, Y.-D. Yang, and X.-B. Yuan, JHEP **06**, 172 (2024), arXiv: 2402.19208
[54] **KOTO** Collaboration, J. K. Ahn *et al.*, Phys. Rev. Lett. **122** (2019), no. 2 021802, [arXiv: 1810.09655].
[55] G. D'Ambrosio, G. Isidori, and J. Portoles, Phys. Lett. B **423**, 385 (1998), arXiv: hep-ph/9708326
[56] A. J. Buras, Eur. Phys. J. C **83**(1), 66 (2023), arXiv: 2209.03968
[57] **KTeV** Collaboration, A. Alavi-Harati *et al.*, Phys. Rev. Lett. **93** (2004) 021805, [hep-ex/0309072].
[58] **KTEV** Collaboration, A. Alavi-Harati *et al.*, Phys. Rev. Lett. **84** (2000) 5279–5282, [hep-ex/0001006].
[59] **Belle-II** Collaboration, L. Aggarwal *et al.*, *Snowmass White Paper: Belle II physics reach and plans for the next decade and beyond*, arXiv: 2207.06307.
[60] W.-F. Wang and Z.-J. Xiao, Phys. Rev. D **86**, 114025 (2012), arXiv: 1207.0265
[61] **Belle, Belle-II** Collaboration, I. Adachi *et al.*, Phys. Rev. Lett. **133** (2024), no. 10 101804, [arXiv: 2404.08133].
[62] M. Beneke, C. Bobeth, and R. Szafron, JHEP **10** (2019) 232, [arXiv: 1908.07011].[Erratum: JHEP 11, 099 (2022)].
[63] **CMS** Collaboration, A. Tumasyan *et al.*, Phys. Lett. B **842** (2023) 137955, [arXiv: 2212.10311].
[64] S. Sahoo, D. Banerjee, M. Kumar, and S. Mohanty, Int. J. Mod. Phys. A **27**, 1250184 (2012), arXiv: 1302.6166
[65] **HPQCD** Collaboration, W. G. Parrott, C. Bouchard, and C. T. H. Davies, Phys. Rev. D **107** (2023), no. 1 014511, [arXiv: 2207.13371]. [Erratum: Phys.Rev.D 107, 119903 (2023)].
[66] **Belle** Collaboration, J. Grygier *et al.*, Phys. Rev. D **96** (2017), no. 9 091101, [arXiv: 1702.03224].[Addendum: Phys.Rev.D 97, 099902 (2018)].
[67] D. Bečirević, G. Piazza, and O. Sumensari, Eur. Phys. J. C **83**(3), 252 (2023), arXiv: 2301.06990
[68] **DELPHI** Collaboration, W. Adam *et al.*, Z. Phys. C **72** (1996) 207–220.
[69] **Belle-II** Collaboration, N. Taniguchi, *Prospects for the Belle II experiment to further elucidate the KM mechanism and beyond*, arXiv: 2401.08250.
[70] **CMS** Collaboration, A. Hayrapetyan *et al.*, Rept. Prog. Phys. **87** (2024), no. 7 077802, [arXiv: 2401.07090].
[71] **LHCb** Collaboration, R. Aaij *et al.*, Phys. Rev. Lett. **127** (2021), no. 15 151801, [arXiv: 2105.14007].
[72] **BaBar** Collaboration, J. P. Lees *et al.*, Phys. Rev. Lett. **118** (2017), no. 3 031802, [arXiv: 1605.09637].
[73] **LHCb** Collaboration, R. Aaij *et al.*, Phys. Rev. Lett. **118** (2017), no. 25 251802, [arXiv: 1703.02508].
[74] P. Ball and R. Zwicky, Phys. Rev. D **71**, 014015 (2005), arXiv: hep-ph/0406232
[75] P. Ball and R. Zwicky, Phys. Rev. D **71**, 014029 (2005), arXiv: hep-ph/0412079
[76] W. J. Marciano and Z. Parsa, Phys. Rev. D **53**(1), R1 (1996)
[77] Y. Grossman and Y. Nir, Phys. Lett. B **398**, 163 (1997), arXiv: hep-ph/9701313
[78] G. Hiller and M. Schmaltz, Phys. Rev. D **90**, 054014 (2014), arXiv: 1408.1627
[79] A. Lenz, U. Nierste, J. Charles, S. Descotes-Genon, A. Jantsch, C. Kaufhold, H. Lacker, S. Monteil, V. Niess, and S. T'Jampens, Phys. Rev. D **83**, 036004 (2011), arXiv: 1008.1593
[80] **ETM** Collaboration, N. Carrasco, P. Dimopoulos, R. Frezzotti, V. Lubicz, G. C. Rossi, S. Simula, and C. Tarantino, Phys. Rev. D **92** (2015), no. 3 034516, [arXiv: 1505.06639].
[81] M. Ciuchini, *et al.*, JHEP **10**, 008 (1998), arXiv: hep-ph/9808328
[82] J. Brod and M. Gorbahn, Phys. Rev. Lett. **108**, 121801 (2012), arXiv: 1108.2036
[83] D. King, A. Lenz, and T. Rauh, JHEP **05**, 034 (2019), arXiv: 1904.00940
[84] J. Albrecht, F. Bernlochner, A. Lenz, and A. Rusov, Eur. Phys. J. ST **233**(2), 359 (2024), arXiv: 2402.04224
[85] **L3** Collaboration, M. Acciarri *et al.*, Phys. Lett. B **412** (1997) 201–209.
[86] **OPAL** Collaboration, P. D. Acton *et al.*, Phys. Lett. B **273** (1991) 338–354.
[87] **ATLAS** Collaboration, G. Aad *et al.*, Eur. Phys. J. C **76** (2016), no. 4 210, [arXiv: 1509.05051].
[88] M. E. Peskin and T. Takeuchi, Phys. Rev. D **46**, 381 (1992)
[89] M. Aiko and M. Endo, JHEP **05**, 147 (2023), arXiv: 2302.11377
[90] C. Baldenegro, S. Hassani, C. Royon, and L. Schoeffel, Phys. Lett. B **795**, 339 (2019), arXiv: 1903.04151
[91] D. d'Enterria, *Collider constraints on axion-like particles*, in Workshop on Feebly Interacting Particles, 2, 2021. arXiv: 2102.08971.
[92] **CHARM** Collaboration, F. Bergsma *et al.*, Phys. Lett. B **157** (1985) 458–462.
[93] J. D. Clarke, R. Foot, and R. R. Volkas, JHEP **02**, 123 (2014), arXiv: 1310.8042
[94] **FCC** Collaboration, A. Abada *et al.*, Eur. Phys. J. ST **228** (2019), no. 2 261–623.
[95] **CEPC Study Group** Collaboration, *CEPC Conceptual Design Report: Volume 1 - Accelerator*, arXiv: 1809.00285.
[96] M. Chrząszcz, M. Drewes, and J. Hajer, Eur. Phys. J. C **81**(6), 546 (2021), arXiv: 2011.01005
[97] **SHiP** Collaboration, C. Ahdida *et al.*, Eur. Phys. J. C **82** (2022), no. 5 486, [arXiv:2112.01487].
[98] **SHiP Collaboration** Collaboration, R. A. *et al.*, CERN-SPSC-2023-033, SPSC-P-369. (2023).
[99] K. Bondarenko, A. Boyarsky, D. Gorbunov, and O. Ruchayskiy, JHEP **11**, 032 (2018), arXiv: 1805.08567
[100] Z. S. Wang, Y. Zhang, and W. Liu, JHEP **01**, 070 (2025), arXiv: 2409.18424